White Rose Research Online

eprints@whiterose.ac.uk
https://eprints.whiterose.ac.uk
Universities of Leeds, Sheffield and York

Deposited via The University of Leeds.

White Rose Research Online URL for this paper:
https://eprints.whiterose.ac.uk/id/eprint/246575/

Version: Accepted Version

Article:
Zhao, B., Kontziampasis, D., Zhou, M. et al. (2026) Precision Injection-Compression Molding and Functional Integration of Hollow Microneedle Microfluidic Chips for Minimally Invasive Continuous Health Monitoring. Small. e76125. ISSN: 1613-6810

https://doi.org/10.1002/smll.76125

Reuse
This article is distributed under the terms of the Creative Commons Attribution (CC BY) licence. This licence allows you to distribute, remix, tweak, and build upon the work, even commercially, as long as you credit the authors for the original work. More information and the full terms of the licence here:
https://creativecommons.org/licenses/

Takedown
If you consider content in White Rose Research Online to be in breach of UK law, please notify us by emailing eprints@whiterose.ac.uk including the URL of the record and the reason for the withdrawal request.

UNIVERSITY OF LEEDS
University of Sheffield
UNIVERSITY of York

Precision Injection-Compression Molding and Functional Integration of Hollow Microneedle Microfluidic Chips for Minimally Invasive Continuous Health Monitoring

Baishun Zhao[a b], Dimitrios Kontziampasis[c], Mingyong Zhou[a], Wangqing Wu[* a](吴旺青), Zhiyu Yang[d], Bingyan Jiang[a], Dou Zhang[* b]

a. State Key Laboratory of Precision Manufacturing for Extreme Service Performance, School of Mechanical and Electrical Engineering, Central South University, Changsha 410083, China

b. State Key Laboratory of Powder metallurgy, Powder Metallurgy Research Institute, Central South University, Changsha 410083, China

c. Institute of Medical and Biological Engineering, School of Mechanical Engineering, Faculty of Science and Engineering, University of Leeds, LS2 9JT, Leeds, Yorkshire, UK

d. Jingmu (Zhuhai) Company Limited, Zhuhai 519055, Guangdong, China

*Corresponding author E-mail address: csuwwq@csu.edu.cn (Wangqing Wu)

dzhang@csu.edu.cn (Dou Zhang)

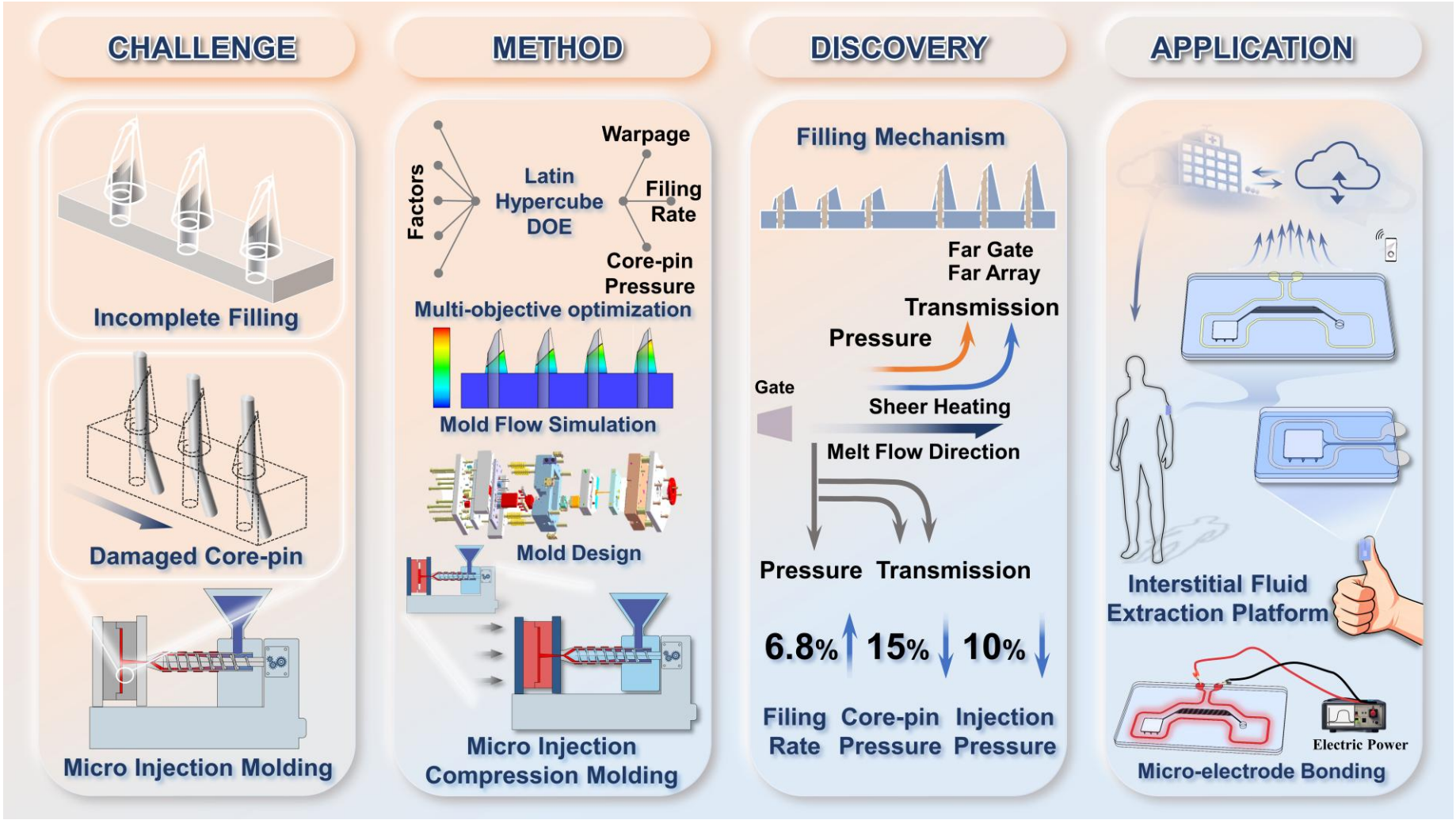
ORCID: B. Zhao: 0000-0001-7530-8630, D. Kontziampasis: 0000-0002-6787-8892, M. Zhou: 0000-0002-7132-4681, W. Wu: 0000-0002-8384-9012, B. Jiang: 0000-0002-5548-3340, D. Zhang: 0000-0001-8555-2784

Abstract

Real-time biomarker monitoring through interstitial fluid (ISF) sampling using hollow microneedle (HMN) arrays is crucial for personalized precision medicine and chronic disease management. However, clinical translation faces a critical bottleneck: the absence of stable, cost-effective, scalable high-precision manufacturing technologies. This work systematically establishes a comprehensive end-to-end solution encompassing precise molding and functional integration. We employed injection-compression molding with multi-objective optimization algorithms to elucidate relationships between critical process parameters and HMN array molding quality. The results demonstrate that positioning the HMN array at the far-gate locations enhances filling quality and reduces core-pin impact force by 15%, revealing the underlying physical mechanisms governed by shear heating effects and pressure transmission dynamics, which enriches conventional micro-injection molding theory. The optimized process achieves >6.8% filling ratio improvement and 10% injection pressure reduction. Furthermore, we established a complete design and fabrication workflow for ISF extraction chips, developed patterned microelectrode bonding technology for complex microchannel sealing and validating in-situ detection platform advantages. In vitro testing validated safe and efficient ISF extraction with a 95% success rate while maintaining exceptional portability for wearable health monitoring applications. This work provides theoretical and practical guidance for scalable HMN manufacturing, establishing a foundation for commercializing next-generation continuous health monitoring systems.

Keywords: Hollow microneedle array, Microinjection molding, ISF extraction, Microfluidic chips, Injection compression molding, Health monitoring platform

Graphic abstract



Highlights

1. Far-gate microneedles: Better filling, lower impact forces—a counterintuitive manufacturing breakthrough.
2. Multi-objective optimization enables cost-effective mass production of high-aspect-ratio hollow microneedle arrays.
3. New filling mechanism expands micro-molding theory beyond conventional near-gate paradigms.
4. First application of patterned microelectrode bonding unlocks in-situ detection in complex microfluidic architectures.
5. Prototype HMN microfluidic platform: 95% success for minimally invasive interstitial fluid extraction.

1. Introduction

Real-time monitoring of physiological biomarkers is increasingly important for personalized medicine, chronic disease management and point-of-care diagnostics [1,2]. Portable, wearable devices and point-of-care testing (POCT) systems capable of providing instantaneous feedback on dynamic biomarker fluctuations have emerged as a research focus in personalized precision medicine [3,4]. These technologies aim to offer users with convenient, non-invasive, or minimally invasive access to health information, thereby enabling early warning and efficient management of chronic diseases such as diabetes and cardiovascular disorders [5].

Although venous blood sampling remains the clinical gold standard, its high invasiveness, limited sampling frequency, and poor patient compliance severely impede the realization of continuous health monitoring. Over the past decade, interstitial fluid (ISF), the biological fluid bathing cells within the extracellular matrix, has emerged as an ideal alternative [6–8]. ISF offers molecular information comparable to blood plasma while substantially reducing invasiveness [9,10]. Comprising approximately 75% of extracellular fluid volume, ISF contains glucose, proteins, electrolytes, metabolites, and even pharmaceuticals diffused from capillaries, and is free from blood coagulation issues or cellular interference, rendering it an ideal medium for real-time health monitoring [11–14]. Consequently, developing a technological "window" for safe, efficient, and minimally invasive ISF collection represents a critical step toward unlocking the full potential of continuous health monitoring [15,16].

Against this backdrop, microneedle technology, particularly hollow microneedle (HMN) arrays with typical lengths of 100-1000 μm, has been explored as a promising minimally invasive platform for ISF sampling. HMNs can penetrate the stratum corneum and access dermal ISF while limiting interaction with deeper nerves and blood vessels, and recent studies have demonstrated HMN-based ISF sampling and biomarker detection [17–19]. These devices leverage internal microchannels to enable a "pierce-and-flow" mechanism while also offering drug delivery capabilities [20,21]. The integration of HMN arrays with microfluidic chips to construct a unified ISF collection and analysis platform holds promise for achieving lab-on-a-chip (LoC) continuous

monitoring [22,23], demonstrating substantial application potential in clinical diagnostics and health management [24,25].

However, despite significant progress in theoretical frameworks and laboratory prototypes, the translation of HMN-based microfluidic chips toward clinical applications and commercial production remains challenging. The core bottleneck lies in the absence of stable, cost-effective, and scalable high-precision molding technologies [26,27]. HMNs possess complex three-dimensional microstructures characterized by high aspect ratios, thin walls, and sharp tips, imposing stringent manufacturing requirements [28,29]. Currently, while photopolymerization-based 3D printing (such as two-photon polymerization) and laser micromachining can achieve exceptional forming precision [30,31], their low production efficiency and prohibitive equipment costs render them unsuitable for mass production. In contrast, micro-molding technologies represented by micro injection molding (μIM) are widely regarded as the viable route for achieving low-cost, high-volume manufacturing of polymer-based microneedles [32,33]. Its advantages are further amplified for materials that are biocompatible (PMMA, PC, COC, etc.) and suitable for injection molding [34]. Nevertheless, conventional μIM processes confront a series of severe and common challenges when replicating intricate structures such as HMNs [32,35]. The high flow resistance of polymer melt within microscale cavities often leads to critical defects—including incomplete filling (short shots), tip blunting, shrinkage-induced distortion, and excessive residual stress [35,36]—which significantly compromise the mechanical integrity and skin-penetration performance of the microneedles [37]. To address these issues, researchers have explored injection-compression molding (ICM) processes, which apply dynamic compression during injection to enhance melt flow and packing behavior within microstructures [38,39], thereby improving replication fidelity. However, even with ICM implementation, the systematic optimization of the process parameter window to balance multiple conflicting molding objectives—including filling ratio, cycle time, injection pressure, and clamping force—remains a complex challenge for fabrication [40]. Furthermore, the substantial impact forces and wear imposed on fragile microcavity core pins by high-pressure injection result in short service life and elevated

maintenance costs [41], representing another critical obstacle to the stable mass production of HMN arrays. Concurrently, one of the most pivotal technological challenges that demands urgent resolution in this field is to achieve reliable bonding and sealing between precisely molded microneedle arrays and substrates containing microchannels and sensing electrodes, in order to construct functionally integrated microfluidic chips [42–44].

This study addresses the critical challenges in precision molding and scalable fabrication of hollow microneedle microfluidic chips through systematic investigation of injection-compression molding. By integrating mold structural design with multi-objective optimization algorithms, we establish precise control over the HMN array molding process and elucidate the complex interactions among critical parameters—gate location, injection speed, packing pressure, and mold temperature. Building upon these findings, we propose an integrated ISF collection microfluidic chip design and develop a complete fabrication workflow incorporating patterned microelectrode bonding technology. This work provides theoretical foundations and practical guidance for low-cost, high-volume manufacturing of high-performance HMN arrays, establishing a pathway toward commercialization of next-generation integrated health monitoring systems.

2. Material and methods

2.1 Material

Poly(methyl methacrylate) (PMMA CM 205, Chi Mei, Taiwan) is used to fabricate microneedle-based microfluidic chips, with its physical properties found in Ref. [45]. Prior to injection molding, PMMA material was dried in an oven at 80°C for over 6 hours to eliminate moisture effects. Nickel (Ni, VALE INCO, Canada) is used to prepare microelectrodes for bonding. The specific formulation of the electroplating solution and the detailed preparation procedure are described in Ref. [46].

2.2 Design of Hollow Microneedle Microfluidic Chips

In applications targeting ISF collection, the HMN array and microfluidic chip are fabricated as an integrated structure through single-step molding. The structural configuration and operational schematic are illustrated in Fig. 1(a). The HMN geometry

and microfluidic chip layout were designed using SolidWorks 2019 (Dassault Systems, France). The design workflow consisted of four steps. First, the target HMN dimensions are defined according to the required skin insertion depth, mechanical stability and ISF collection volume. Second, a 3 × 3 HMN array is constructed with an inter-needle spacing of 2 mm to reduce the bed-of-nails effect while maintaining sufficient sampling area. Third, the lumen outlet is shifted from the central puncture axis to reduce the risk of tissue coring and channel blockage during insertion. Finally, the HMN array is integrated with microchannels, a collection chamber and chip-level fluidic structures to form the complete ISF collection device. The detailed design basis and process are developed in Section 3.1.

The Young-Laplace-based capillary-pressure equations are used to evaluate the feasibility of passive liquid transport within the rectangular microchannels [47,48], as shown in Fig. 1(b).

$$\Delta P = \gamma \left(\frac{\cos\theta_t + \cos\theta_b}{h} + \frac{\cos\theta_l + \cos\theta_r}{w} \right) \tag{1}$$

where ΔP represents the capillary pressure (MPa); γ denotes the surface tension of the liquid within the microchannel (N/m); h and w represent the channel height and width (m), respectively; and θ_t, θ_b, θ_l, and θ_r correspond to the contact angles between the liquid and the top, bottom, left, and right walls of the microchannel, respectively.

For microchannels with identical wall materials on all four surfaces, the equation simplifies to:

$$\Delta P = 2\gamma \cos\theta \left(\frac{1}{h} + \frac{1}{w} \right) \tag{2}$$

Equation 2 reveals that capillary pressure increases with decreasing microchannel dimensions, exhibiting an inverse relationship with the characteristic dimension (e.g., hydraulic diameter).

These equations guide the selection of microchannel dimensions and help determine whether capillary pressure is sufficient to drive fluid movement after ISF entered the chip. Therefore, the equations are used as a microfluidic design criterion, whereas the HMN geometry is determined by the combined requirements of skin insertion,

mechanical strength, mold-core manufacturability and ISF collection.

2.3 Static and Mold Flow Simulation

The Static Structural module in Ansys Mechanical (version 2020 R2, ANSYS Inc.) is employed to validate microneedle structural integrity through finite element analysis. Simulations evaluate stress distribution and deformation under operational loads. During preprocessing, mesh discretization utilizes tetrahedral elements with a size of 15 μm (see Fig. 1e), totaling 157,426 elements—sufficient to satisfy static simulation requirements. The constitutive equation for PMMA is represented by a Maxwell viscoelastic model derived from experimental measurements and curve fitting, with model parameters and construction procedures from literature [34]. Studies have demonstrated that an insertion force of approximately 0.2 N per needle is sufficient for effective human skin penetration without causing excessive pain or tissue damage [49]. Consequently, a force of 0.2 N is applied as the validation pressure for the HMNs, with additional boundary conditions as shown in Fig. 1(f).

The mold flow simulation model for hollow microneedle micro-injection molding is constructed at a 1:1 scale based on the designed gating system, as shown in Fig. 1(g). Simulations are performed with Moldflow Synergy 2018 (Autodesk, USA). Mesh discretization employed tetrahedral elements, with an initial global mesh size of 0.5 mm subsequently refined through optimization.

2.4 Hollow Microneedle Array Injection Compression Molding

Injection-compression molding (ICM) is employed to overcome scale effects and reduce the flow length-to-thickness ratio. ICM enhances product molding precision by applying compressive force following melt injection into the mold cavity, as illustrated in Fig. 1(h). An Arburg precision micro-injection molding machine (370S, Arburg, Germany) is utilized to conduct HMN array injection molding and injection-compression molding experiments. A mold temperature controller (AOSD-05A, China) regulates mold body temperature, while a desiccant dryer (SCD-20U/30H, China) is employed for raw material drying.

2.5 Experimental design of injection and injection compression molding

Given the advantages of optimized Latin hypercube sampling in achieving uniform

distribution of variable sampling points, this method is adopted for experimental design. The sampling scheme is generated using Isight 2016 (Simulia, France), and the corresponding experimental factors and parameter combinations are listed in Tables S1 and S2 (Supplementary material). For each parameter combination, numerical simulations are performed to extract three response variables: the HMN cavity filling rate, the warpage deformation of the thin-walled component, and the maximum pressure acting on the mold core pin. The relative contribution of each processing parameter to these responses is then evaluated using Pareto analysis. Specifically, the absolute effect of each parameter on a given response is normalized by the sum of the absolute effects of all investigated parameters and expressed as a percentage contribution.

Due to the small dimensions and precise geometry of hollow microneedles, even minor deviations in process parameters significantly affect the accuracy of the final product. For ICM, the pressure and timing control during the compression stage must be perfectly coordinated with the injection process to ensure structurally complete and defect-free HMN formations. Therefore, the HMN injection molding experiments are conducted in two phases. Firstly, injection molding experiments are performed based on optimized parameter combinations, followed by the introduction of compression-stage processing parameters (parameter combinations are listed in Table 1). Each parameter combination is repeated 50 times, and five samples are randomly selected from the final 40 cycles for statistical analysis of molding precision and process stability.

Table 1. The injection and ICM process parameters of hollow microneedle microfluidic chip

Process	ICM								
	Injection molding (Injection stage)					Compression stage			
Factor	IS	IP	MT	PP	Mold T	PT	CD	CS	CF
Unit	cm^3/s	MPa	℃	MPa	℃	s	mm	mm/s	MPa
Range	40-50	120-160	270-275	120-160	90	3	1	5	450

Note: Injection speed (IS), Injection pressure (IP), Melt temperature (MT), Packaging pressure (PP), Mold temperature (Mold T), Packaging time (PT), Compression Distance (CD), Compression speed (CS), Compression force (CF)

2.6 Morphology characterization of hollow microneedle array

The three-dimensional morphology of hollow microneedles is characterized using an

ultra-depth 3D microscopy system (KEYENCE® VHX-5000, Japan). Detection parameters and settings included 100× magnification, image stitching, and ring illumination. Five random replicates are selected under identical injection parameters for statistical analysis.

The coefficient of variation (CV) is used to describe sample consistency and uniformity (Eq. 3). In practical applications, the CV is commonly employed to evaluate the precision of experimental methods, the stability of production processes, and the uniformity of sample preparation. A CV below 5% indicates excellent sample consistency, 5-10% indicates good consistency, 10-15% indicates moderate consistency, and values exceeding 15% indicate poor consistency.

$$CV = \frac{\sqrt{\frac{1}{n}\sum_i^n (x_i - \bar{x})^2}}{\frac{1}{n}\sum_i^n x_i} \times 100\% \quad (3)$$

where, n represents the number of samples, $\bar{x}$ denotes the sample average.

2.7 Mechanics and puncture performance

The mechanical properties of microneedles are evaluated using a micro-mechanical tensile-compression tester (PT-1198GTD-P, Boda Instrument, China), at a loading rate of 1 mm/s. Testing was terminated when the applied force reached 40 N. A total of 5 replicate groups are tested for HMN strength characterization. Sensors are calibrated prior to testing to ensure measurement accuracy.

Porcine and human skin exhibit highly similar dermal/epidermal layer ratios, hair follicle and blood vessel densities, and dermal collagen/elastin ratios [50]. Fresh porcine dorsal skin, harvested within 24 hours post-mortem, was procured from a morning market near the laboratory. Prior to use, the porcine skin was thoroughly rinsed with warm physiological saline to remove blood, adipose tissue, and surface contaminants. Excess fat and muscle tissue were removed while preserving a portion of the dermal layer. To facilitate marking and statistical analysis, ink is injected into the HMN array cavities to serve as a penetration dye. It is important to note that penetration staining experiments are repeated 9 times.

2.8 Preparation of Hollow Microneedle Microfluidic Chip

Microchannels, capillary pumps, and capillary diffusion regions are fabricated using a CO_2 laser engraving system (Young Laser V12, China). For microchannels and capillary pump regions, vector engraving mode is employed with laser intensity at 30% full power and scanning speed of 15 mm/s. For capillary diffusion regions, raster engraving mode is utilized with laser intensity at 40% full power and scanning speed of 15 mm/s. Absorbent paper (Beckman, China), composed of neutral cotton fiber material with ash content below 0.15%, is subsequently cut and prepared according to the required structural configurations.

The microfluidic chips are bonded using a novel patterned microelectrode bonding process [46]. A power supply unit (Agilent B2901A, Keysight, USA) is employed for microelectrode fabrication and bonding.

According to different bonding schemes for ISF analysis platforms, electrodeposition masks are fabricated using the laser engraving system. Mask preparation used vector engraving mode with laser intensity at 15% full power and scanning speed of 20 mm/s. The cross-sectional dimensions of different microelectrodes remain rectangular at 600 × 40 μm, with electrodeposition processing parameters including an electrode spacing of 10 cm, current density of 4 A/dm², and deposition time of 45 minutes.

2.9 Artificial blood collection

Artificial blood (YT-062, China) is employed as a surrogate for human or animal experimentation to characterize the ISF extraction capability of hollow microneedles. Artificial blood possesses physical properties similar to those of blood, including surface tension and viscosity, with primary constituents comprising amaranth dye, surfactants, thickening agents, inorganic salts, and distilled water. The use of artificial blood provides standardized fluid characteristics, facilitating enhanced experimental control and improved data reproducibility. The liquid absorption capacity of capillary pumps is evaluated by comparing artificial blood flow distances over identical time intervals.

2.10 In vivo ISF collection and skin-response assessment

An exploratory animal study is conducted by Hangzhou Yanqu Information Technology

Co., Ltd., Hangzhou, China. Animal experiments were approved by the Lab of Animal Experimental Ethical Inspection of Dr.Can Biotechnology(Zhejiang) Co., Ltd., China (Approval No. DRK-20260702042). Two male Institute of Cancer Research mice (6-8 weeks old, 18-22 g) are acclimatized for 3 days before testing. The mice are randomly designated as animals A and B, and each animal received one Case I HMN device. For in vivo ISF extraction, the dorsal hair of mice is removed before testing, and the HMN device with a collection layer is placed on the exposed dorsal skin. The extraction process is photographed at 0, 10, 20, 30 and 40 min. After device removal, the puncture sites are photographed at 0, 10, 20 and 30 min to evaluate short-term skin recovery. Skin from the other animal is collected immediately after HMN application, before visible closure of the puncture sites. The tissue is paraffin-embedded and stained with haematoxylin and eosin (H&E) for histological examination. Because this experiment is designed as an exploratory feasibility assessment with two animals, the outcomes are analyzed descriptively without inferential statistical testing.

3. Results and discussion

3.1 Hollow Microneedle Structural Design and Simulation

Hollow microneedle microfluidic chips integrate the advantages of HMN arrays and microfluidic technology, enabling precise and controlled drug delivery as well as ISF collection [51,52]. Microneedle-assisted biosensing applications have demonstrated that capillary action facilitates analyte detection in liquids [53]. Numerous related studies have further shown that microneedles can extract blood and ISF through capillary action alone, without requiring additional negative pressure (suction) devices [54,55]. For single-step in-mold fabrication and user convenience, achieving ISF extraction through capillary pump design represents an optimal approach [56–58].

Interstitial fluid is rich in metabolites, proteins, and other biomolecules; consequently, ISF collection enables non-invasive or minimally invasive health monitoring and disease diagnostics [59]. For ISF collection applications, microneedle dimensions and geometry directly determine collection efficiency and user comfort. Microneedle size, shape, tip radius, needle height, base width, overall design, and geometric configuration are critical for enhancing mechanical performance and strength, while they directly

influence adequate insertion depth and structural integrity [60,61].

The structural composition and thickness relationships of human skin tissue are illustrated in Fig. 1(c). In ISF extraction applications, consideration must be given to the three distinct layers of human skin: the stratum corneum (10-20 μm) [62], epidermis (100-150 μm) [63], and dermis (3-5 mm) [64]. Consequently, HMN height must exceed 200 μm to reach the dermal layer and achieve ISF collection. A strong correlation exists between microneedle length and pain perception. Reports indicate that pain increases more than sevenfold as microneedle length increases from 480 μm to 1450 μm [65]. Therefore, longer microneedles are more likely to activate nociceptors or puncture capillaries, causing bleeding and potentially reducing user acceptance [66]. Additionally, most microneedles maintain heights below 1 mm whilst remaining sufficient for ISF collection or therapeutic agent delivery [67]. Thus, an ideal microneedle height approximates 1 mm.

It is self-evident that microneedle geometry substantially determines mechanical strength. Microneedles can adopt conical, pyramidal, cuboidal, triangular prismatic, or cylindrical configurations. It has been proven that, cylindrical microneedles can withstand greater loads compared to square or rectangular microneedles of equivalent cross-sectional area [68]. Compared to pyramidal hollow microneedles, conical tips exhibit superior mechanical stability, reduced bending deformation, and higher internal flow rates [69]. In practical design processes, optimization and trade-offs must be made according to specific application scenarios and manufacturing processes. To achieve mass production, micro-injection molding technology is employed for HMN array fabrication. Therefore, the conical profile is preferred as it facilitates demolding [70].

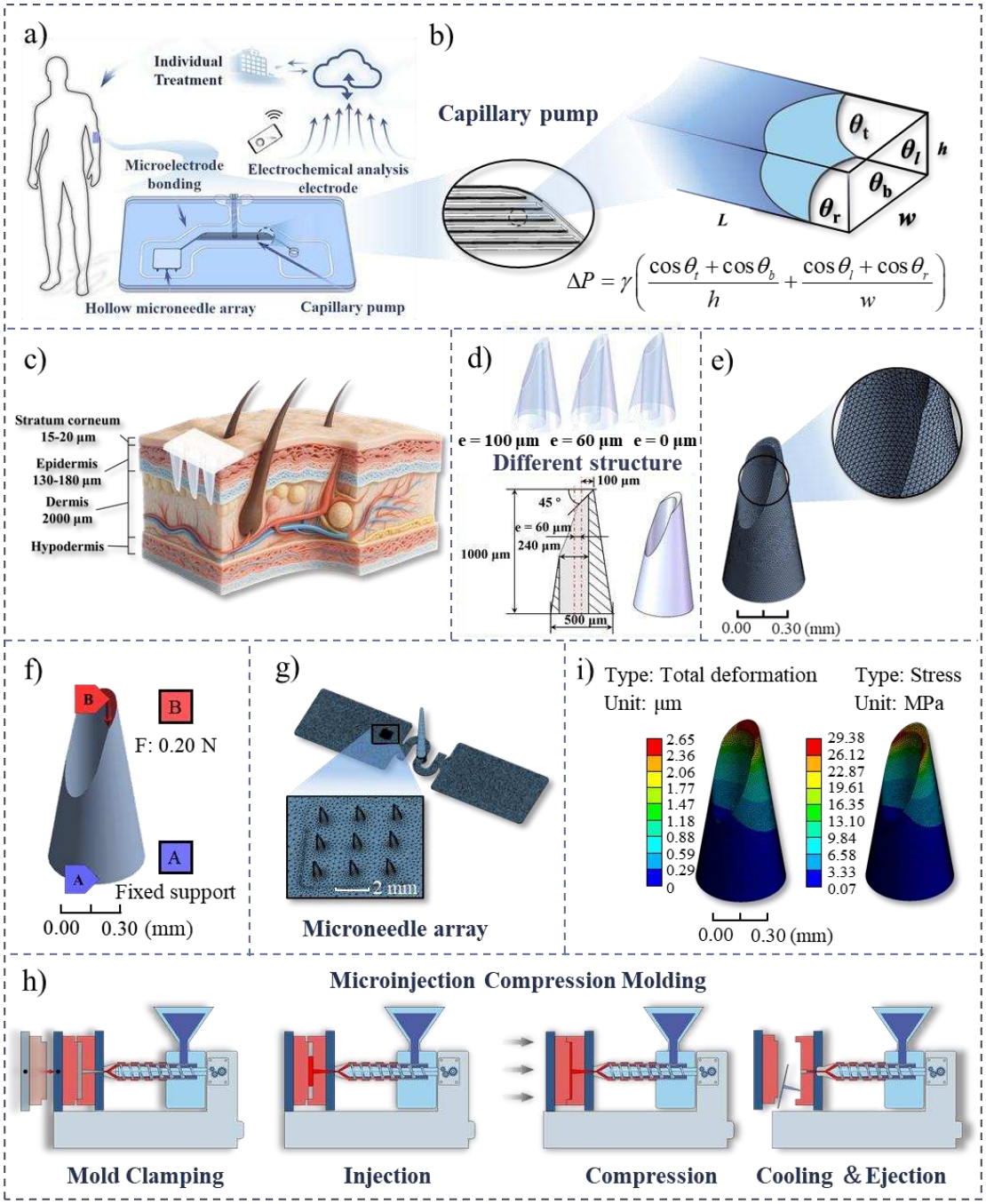


Fig. 1. Design, fabrication, and mechanical characterization of microneedle arrays for ISF extraction via microinjection compression molding. (a) Schematic illustration of the ISF-based health monitoring system. (b) Geometric design and capillary pressure calculation model for the capillary pump. (c) Cross-sectional anatomy of human skin showing the target insertion depth for microneedles. (d) Microneedle geometric specifications and structural variations. e: distance between hollow-channel axis and conical microneedle axis. (e) Detail and quality of local mesh division of microneedles. (f) Finite element analysis setup for mechanical testing simulation. (g) 1: 1 gating system model and mesh generation for mold flow simulation. (h) Microinjection compression molding (μICM) fabrication process flow. (i) Finite element simulation results showing mechanical performance under compressive loading.

According to studies on cutaneous nerve ending distribution density, when microneedle diameter falls below 200 μm, penetration can avoid most nerve endings, significantly reducing pain sensation. As diameter increases, the needle inflicts greater damage area on the skin, substantially elevating pain perception [65]. For conical structures, wider base/support structures provide higher mechanical stability, with these diameters typically on the order of 300-700 μm. For hollow microneedles, sufficient sharpness is required to reduce insertion force. Consequently, beveled or polyhedral designs can be considered to minimize insertion resistance, with tip angles typically ranging between 15-45°. Furthermore, flat hollow tips may impede fluid flow due to tissue coring during skin perforation [71]. Therefore, an eccentric structure was designed for the HMNs; this structural configuration effectively prevents microneedle clogging while ensuring adequate biofluid collection volume. The hollow channel can exploit capillary action to facilitate ISF collection. Fig. 1(d) illustrates the structural evolution and key geometric parameters of the hollow microneedles. Three hollow microneedle configurations are designed by varying the eccentric distance, e, between the central axis of the hollow channel and the central axis of the outer conical microneedle body. The eccentric distances are set as e = 100 μm, 60 μm, and 0 μm. The e = 0 μm structure represents a coaxial hollow microneedle, while the e = 60 μm and e = 100 μm structures represent eccentric hollow microneedles with different degrees of lateral channel displacement. The final eccentric beveled design further shifts the lumen outlet away from the central puncture axis, thereby reducing the probability that compressed tissue directly enters and blocks the lumen while maintaining sufficient collection volume for interstitial fluid. The principal geometric parameters are set as follows: needle height, 1000 μm; base diameter, 500 μm; upper base radius,100 μm; lumen diameter, 240 μm; chamfer angle, 45°; and eccentric offset, 60 μm. These dimensions are selected by considering skin insertion, structural stability, capillary-driven ISF collection, mold-core strength, and fabrication feasibility.

Beyond individual HMN structure and dimensions, microneedles are typically applied in array configurations. Consequently, the bed-of-nails effect must be considered during array structural design, wherein needles arranged in an array positioned too closely

together fail to penetrate skin [72]. Theoretical analysis demonstrates that insertion force decreases with increasing spacing. As spacing increases beyond 150 μm, the correlation between insertion force and needle pitch progressively diminishes [73]. Simultaneously considering HMN mold manufacturing cycle and cost, a 9-needle HMN array is exemplified here, with inter-needle spacing set at 2 mm. Without considering subsequent microchannels and storage chamber volumes, the theoretical ISF extraction capacity of the HMN array structure approximates 7.71 μL.

Finite element simulation is employed to validate the mechanical strength of the designed HMNs. Under a 0.2 N load, the stress distribution of the HMN exhibits pronounced gradient variations, indicating favorable mechanical performance under loading conditions (see Fig. 1(i)). Relatively higher stresses are observed on the inner walls, attributable to the geometric characteristics of the hollow structure that concentrate stress in regions of reduced wall thickness. Even if stress concentration at the tip is relatively pronounced, the maximum stress (24.86 MPa) does not exceed the material yield strength (65±3 MPa), confirming that the design satisfies mechanical strength requirements. Deformation under loading manifests most significantly at the microneedle tip as illustrated in the Fig. 1(i). However, the overall structure maintains high rigidity without evident buckling or fracture risk. Concurrently, the overall deformation remains minimal, with maximum displacement of merely 2.2 μm (see Fig. 1(i)), demonstrating sufficient structural rigidity to preserve shape during skin insertion, thereby ensuring successful ISF collection.

3.2 Simulation of injection molding and mold design

The complex structure and high aspect ratio of hollow microneedles render mold design critically important. During injection-compression molding, the mold must incorporate precision core pin structures to form the through-hole features of HMNs. For both solid and hollow microneedles, gas entrapment represents a principal cause of incomplete microstructure filling. Specifically, when molten material fills the microneedle mold cavity, failure to timely evacuate internal air results in gas retention (gas pockets), impeding melt flow and causing insufficient filling. Due to the fine internal channels within HMN structures, gas entrapment occurs more readily, obstructing polymer

material filling. Consequently, enhancing mold venting capability is recognized as critical for achieving precision microneedle molding [74].

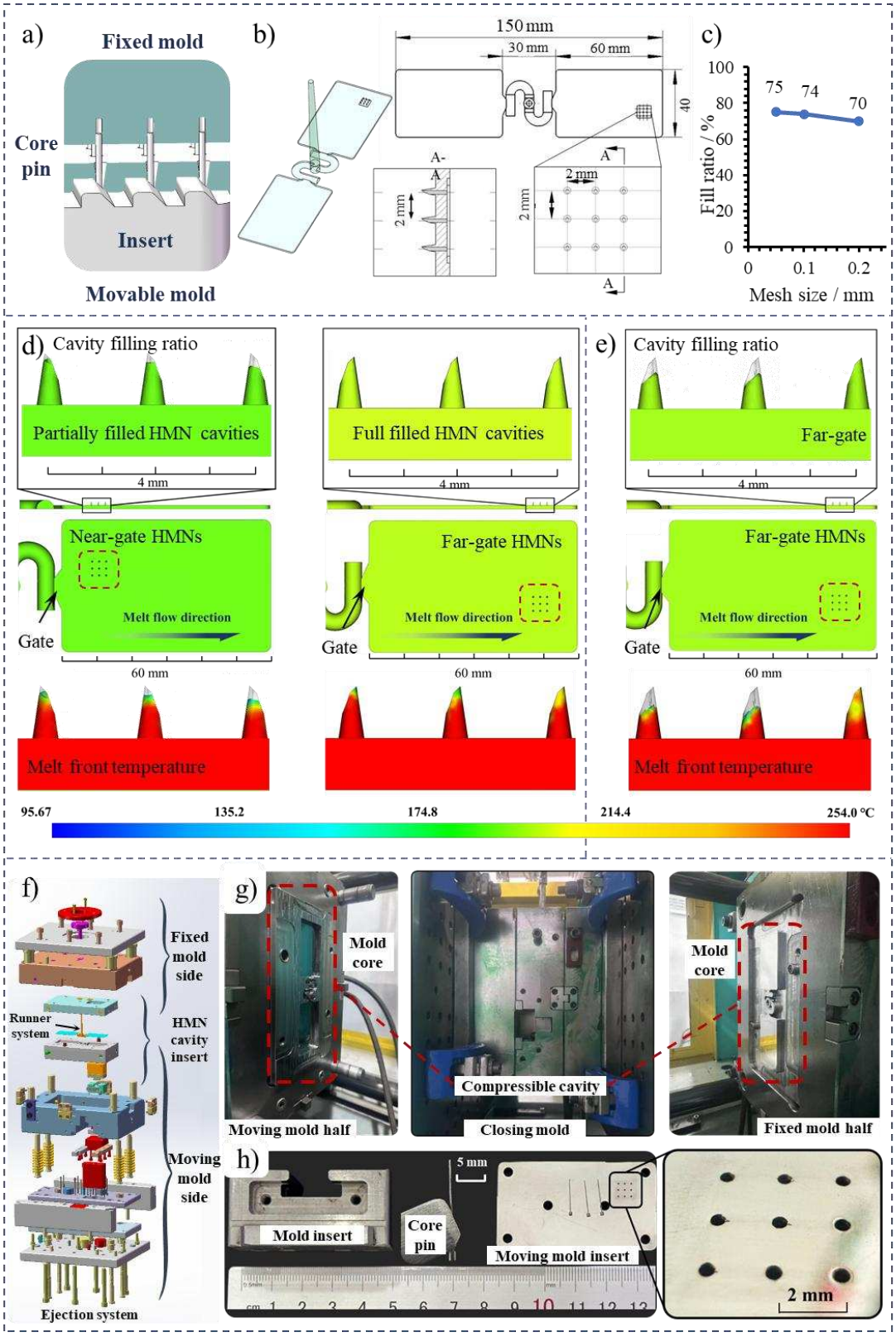


Fig. 2. Mold design, thermal simulation, and manufacturing system for μICM of microneedle arrays. (a) Cross-sectional schematic of the mold assembly for microneedle fabrication. The system consists

of a fixed mold (upper, teal) containing core pins that define the hollow channels, and a movable mold (lower, gray) with insert cavities that shape the external microneedle geometry. (b) Detailed mold design specifications and runner system layout. (c) Mold cavity fill ratio as a function of mesh size in mold flow simulation. (d) Effect of gate position on filling ratio and melt front temperature under identical process conditions. (e) Under short-shot conditions (No. 10 in Table S2), the microneedle cavity farthest from the gate fills first. (f) Exploded view of the complete microinjection compression molding system assembly. (g) Photographs of the industrial-scale μICM equipment during operation. (h) Fabricated mold inserts and core pins. The high-quality surface finish and dimensional accuracy contribute to precise molding.

Compared to mold cores fabricated monolithically through casting or laser engraving techniques, assembling critical components to form a mold core assembly offers superior breathability. Based on a chip substrate with dimensions of 60 mm length × 40 mm width × 1 mm thickness, the designed HMN microfluidic chip mold core assembly is illustrated in Fig. 2(a). This design approach is more streamlined and systematic, facilitating machining and maintenance while ensuring uniform material filling during molding, thereby reducing the occurrence of gas pockets and defects.

Fig. 2(b) presents the designed gating system for the HMN microfluidic chip. For thin-walled components, circular and semicircular cross-section runners represent relatively rational design choices. These runner configurations possess smaller surface area-to-volume ratios, maximally minimizing flow friction and heat loss of the material [75]. Consequently, considering runner volume and balanced runner design principles, an S-shaped semicircular interface runner structure with central symmetry about the main runner is designed. Fan gates facilitate more uniform and efficient material distribution throughout the entire mold cavity; for large-area thin-walled components in particular, they effectively enhance molding quality [75]. The aforementioned design principles maximize filling efficiency during thin-walled component molding, reduce defects, and improve product quality and consistency.

Subsequently, mold flow simulation analysis is conducted using Moldflow for both injection molding and injection-compression molding processes to optimize chip structure and molding parameters. Mesh independence (mesh convergence) analysis is performed with mesh refinement applied to the HMN array region. Mesh element sizes are progressively reduced to 0.2, 0.1, and 0.05 mm. Results demonstrate a reverse analogous relationship between element size and microneedle filling ratio. However,

when element size decreases from 0.10 mm to 0.05 mm, the change in filling ratio becomes gradual (increasing from 74% to 75%) (Fig. 2(c)). This indicates that at 0.10 mm mesh size, the mesh discretization adequately describes the flow behavior of the microneedle structure, with limited improvement achieved through further element size reduction. Comprehensively considering computational accuracy and efficiency, selecting a mesh discretization with element size of 0.10 mm (total mesh count approximately 3.39 million) ensures calculation result precision while avoiding computational resource waste.

Under general injection conditions, when microstructure positions are proximal to the gate, the melt flow path is short, temperature and pressure losses are minimal, and microstructure filling ratios are typically high. As the distance between the HMN array and gate position increases, the melt traverses a longer path with increased flow resistance. Pressure loss progressively increases, causing melt pressure at the flow front to gradually attenuate, resulting in incomplete microcavity filling.

However, injection molding results for HMN arrays on thin-walled components exhibit a contrasting molding trend. Under identical injection processing conditions (melt temperature 250°C, mold temperature 80°C, injection speed 20 cm^3/s), HMN arrays positioned near the gate demonstrate significantly lower filling ratios compared to far-gate positions (Fig. 2(d)). This pattern is consistently observed across other process parameter combinations. The mechanisms underlying this phenomenon are as follows: (1) During thin-walled micro-injection molding, viscous dissipation effects elevate melt temperature at the flow front, reducing melt viscosity and creating favorable conditions for HMN cavity filling. Melt flow front temperature distributions at near-gate and far-gate array locations are presented in Fig. 2(d). Results confirm that melt temperature at the far-gate position is markedly higher than at the near-gate position. (2) When HMN array positions are proximal to the gate, microneedle cavity resistance substantially exceeds that of thin-walled cavities, although the melt flow path is short with minimal temperature and pressure losses. This causes melt to preferentially flow toward lower-resistance thin-walled regions rather than into microneedle cavities. As the flow path lengthens, viscous dissipation elevates melt flow front temperature while near-gate

region melts temperature decreases. When melt reaches the thin-walled cavity terminus, elevated melt temperature causes rapid pressure buildup within the cavity, thereby enhancing microstructure filling capability at the far-gate position. Fig. 2(e) further illustrate this filling mechanism under intentionally reduced filling conditions, where a short-shot state was generated to visualize the melt filling sequence (No. 10 in Table S2). The short-shot result shows that the melt first advanced through the lower-resistance thin-walled cavity, whereas the HMN microcavities remained partially filled at the early filling stage. As the melt front approached the far-gate region, viscous dissipation increased the local melt temperature and promoted pressure buildup near the terminal thin-walled cavity, thereby improving the filling capability of the far-gate HMN cavities. This result supports the conclusion that the far-gate position is more favorable for HMN array filling under the present thin-walled micro-injection molding conditions. Based on the above findings, the HMN array is chosen to be positioned at the far-gate.

Integrating simulation analysis results with mold design theory, a mold capable of accommodating both injection molding and injection-compression molding is designed and fabricated. Its three-dimensional exploded view and physical photographs are presented in Figs. 2(f) and (g), respectively. In parallel, the potential medical applications of HMN microfluidic chips impose stringent surface finish requirements. For this reason, the mold core surface roughness is designed and manufactured to mirror-grade quality, i.e. surface roughness ~0.16 μm, (see Fig. 2(g)). To form the hollow structure of microneedles, precision fabrication of metal core pins with 0.24 mm diameter and 6 mm length represents a critical factor ensuring accurate HMN molding. Core pins are fabricated using micro-milling processes, with Ti6Al4V selected as the core pin material due to its moderate hardness, avoiding accelerated tool wear or material deformation during milling. To ensure the tool could handle micro-scale machining, a 500 μm diameter carbide micro-milling cutter is employed. Fig. 2(h) presents the finally fabricated microcavities and core pins.

3.3 Multi-objective process optimization of injection molding

During the injection molding process, the temporal evolution of pressure experienced

by individual core pins at near-gate and far-gate positions is presented in Figs. 3(a) and (b), respectively. Results demonstrate that positioning the HMN array at the far-gate location not only enhances HMN filling ratio but also reduces pressure exerted on mold core pins by 15%. This phenomenon indicates that placing the HMN array at the far-gate position, in addition to improving filling ratio, favorably extends mold core pin service life, serving a protective function for the core pins.

In multi-objective optimization of HMN microfluidic chip micro-injection molding, selecting appropriate optimization indicators is critical for ensuring microneedle functionality, processing efficiency, and product quality. Given the precise structural configuration of HMNs, excessive height deviation may prevent microneedles from penetrating skin or cause user discomfort. Consequently, microneedle cavity filling ratio represents a key indicator affecting product integrity and performance. Chip warpage influences the overall geometry and functional performance of both microneedles and chips. Core pin mechanical strength constitutes a critical factor for maintaining HMN structural integrity and a necessary indicator for ensuring injection molded product quality, safety, and stability. In summary, the optimization indicators considered in this section include HMN filling ratio, chip warpage, and core pin pressure, achieving objectives that balance high performance and economic feasibility for HMN microfluidic chips.

Using chip filling ratio, warpage, and core pin pressure as response indicators, Pareto charts depicting the influence of various process parameters on these response indicators are presented in Figures 3(c-e). Fig. 3(c) reveals the differential contributions of process parameters to filling ratio. The primary influencing factors are injection pressure (32.01%), packing pressure (31.94%), and melt temperature (19.17%), while injection speed, mold temperature, and packing time exert relatively minor influences. Injection pressure and packing pressure exhibit the greatest impact on filling ratio, contributing 32.01% and 31.94%, respectively. This indicates that pressure control represents a critical factor for ensuring adequate filling of HMN cavities and flow channels during injection molding. Higher pressures enable molten polymer material to fill complex mold structures more rapidly and uniformly, reducing defects such as voids

and short shots. Melt temperature influences filling ratio by 19.17%, showing that elevated melt temperatures enhance material flowability, reduce flow resistance, and thereby improve filling performance. Appropriate temperature ensures material does not solidify prematurely, particularly within the fine channels of HMN structures. Injection speed and mold temperature contribute 10.26% and 5.17%, respectively, representing secondary influences. Increased injection speed accelerates the filling process; however, excessive speed can induce air entrapment or weld lines. The limited influence of mold temperature suggests its relatively constrained effect on filling ratio within the given process parameter range. Packing time demonstrates minimal impact on filling ratio at merely 1.45%, likely because the packing stage during injection exerts limited influence on final filling completion, serving primarily to solidify material and reduce shrinkage.

Fig. 3(d) demonstrates the influence of various process parameters on warpage deformation. Mold temperature (35.53%) and injection pressure (30.22%) are the primary factors affecting the warpage deformation, while packing pressure, melt temperature, packing time, and injection speed exert secondary influences. Mold temperature, accounting for 35.53%, represents the most dominant factor influencing warpage deformation, indicating that non-uniform mold temperature distribution can cause differential cooling rates, subsequently generating residual stresses that induce warpage. Both excessively high and low temperatures adversely affect part dimensional stability, particularly in high-precision microneedle structures. Elevated injection pressure can induce non-uniform stress distribution within the mold cavity, especially in complex microstructures, where stress differentials can lead to warpage. Rational pressure control is a key factor in warpage reduction. Packing pressure can mitigate material shrinkage during solidification, thereby partially reducing warpage risk (14.53%). Although these parameters exert secondary effects, they may still serve fine-tuning functions under specific conditions and for precision engineering purposes.

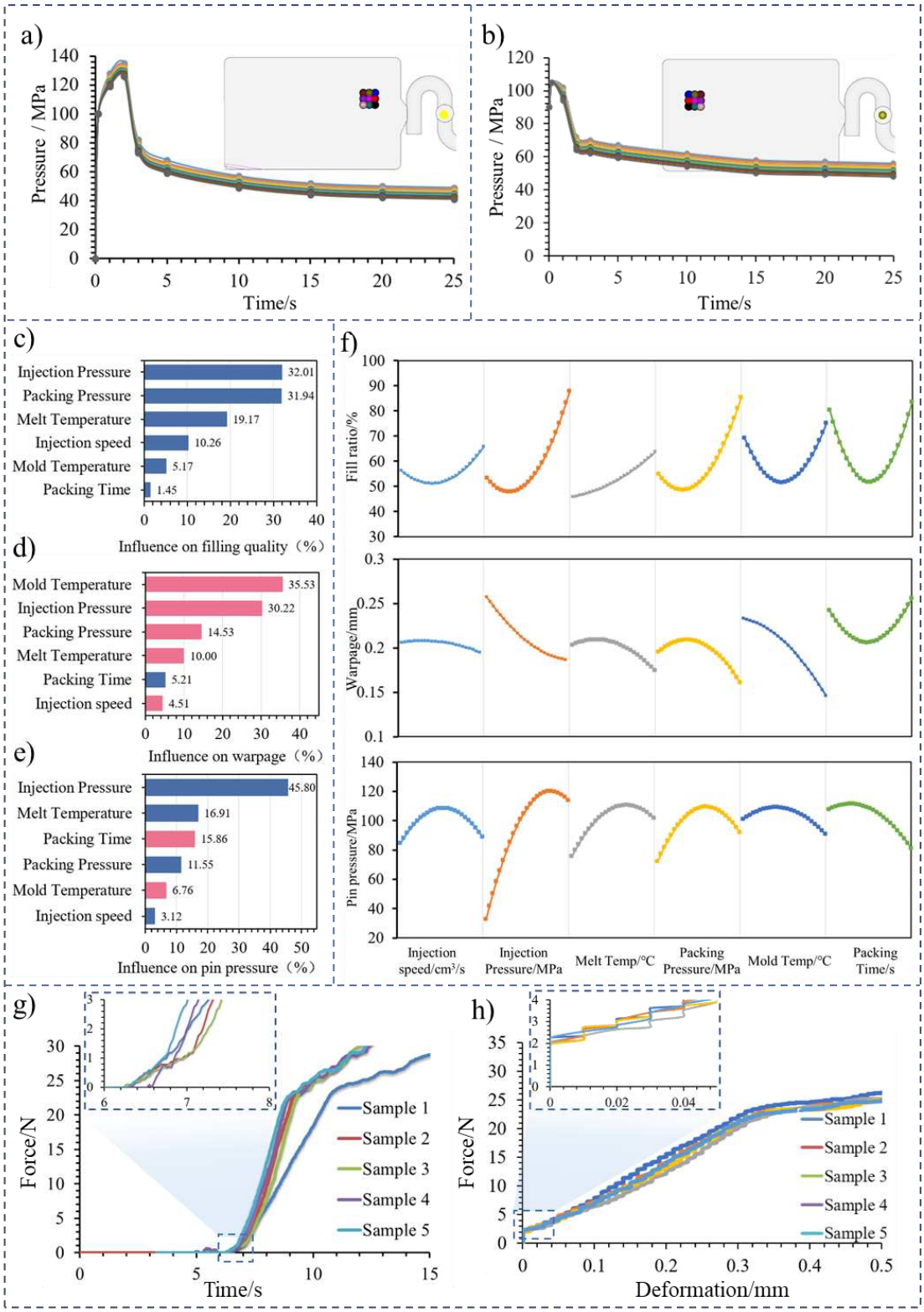


Fig. 3. Process parameter optimization and mechanical characterization of HMN fabricated by microinjection molding. Temporal evolution of melt impact pressure on the core pin at different position ((a) near-gate, (b) far-gate) during the injection molding. The pressure on the core pin at the far-gate is reduced by 15%. (c) Pareto analysis of process parameter influence on (c) filling quality, (d) chip warpage and (e) core pin pressure. Different factors have different influences and laws on different indicators. Blue: positive factor. Pink: negative factor. (f) Main effect diagram of

each experimental factor (See Table S2 for detailed parameter) on different indicators. (g) Force-time curves during axial compression testing of microneedle arrays. Five representative samples (Samples 1-5) show consistent mechanical behavior with initial elastic loading, reaching failure forces between 25-32 N at approximately 6-8 seconds. (h) Force-displacement curves from axial compression tests. The HMN array is deformed when the average test pressure reaches 2.314 ± 0.163 N.

The influence of process parameters on the impact force experienced by mold metal core pins exhibits pronounced differentiation, as illustrated in Fig. 3(e). The primary influencing factor is injection pressure (45.80%), followed by melt temperature (16.91%) and packing pressure (15.86%), while packing time, mold temperature, and injection speed exert minor influences. Injection pressure constitutes the most dominant factor affecting core pin loading at 45.80%, indicating that higher injection pressure results in greater melt impact force on metal core pins. Elevated injection pressure facilitates material filling; however, excessive pressure may cause core pin deformation or even damage. Consequently, effective injection pressure control must be implemented while ensuring filling quality to protect mold component integrity. Melt temperature influences core pin loading by 16.91%. Since at elevated temperatures, material exhibits superior flowability with relatively reduced impact force on core pins during flow. Packing pressure contribution shows that the material continues to exert pressure on core pins during the packing stage. Although this stage exerts limited influence, attention remains warranted since excessive packing pressure may similarly damage the core pins. Packing time, mold temperature, and injection speed have influences of 11.55%, 6.76%, and 3.12%, respectively. These parameters exert secondary effects on core pin loading, primarily manifesting through influences on core pins during localized material flow and solidification processes.

Referencing simulation results based on Latin hypercube experimental design, the main effects plots of various process parameters on response indicators are presented in Fig. 3(f) (specific abscissa parameters detailed in Table S2). With increasing injection pressure and packing pressure, filling ratio exhibits an initial decrease followed by a significant increase. This trend indicates that within a certain pressure range, low pressure causes insufficient melt filling of the mold cavity, resulting in lower filling ratios. Beyond a critical threshold, higher injection pressure substantially improves

filling performance. Rational pressure control can prevent short shot defects. Additionally, packing pressure primarily serves to replenish material and reduce shrinkage, also corroborating from an alternative perspective the conclusion that fan-gate HMN arrays achieve higher filling ratios.

The melt temperature curve displays a gradual ascending trend, indicating that increasing melt temperature facilitates filling ratio enhancement, albeit with less pronounced effects compared to injection and packing pressures. The influence of melt temperature on filling ratio exhibits evident nonlinear behavior. As temperature increases, filling ratio initially rises then declines. This is attributed to insufficient material flowability at excessively low temperatures, whereas at excessively high temperatures, material becomes overly fluid, readily producing excessive flow or flow instability. Packing time exerts minimal influence on filling ratio, with curve variations of limited magnitude. This demonstrates that filling ratio is predominantly controlled by the injection stage, while packing time primarily compensates for material shrinkage.

Mold temperature exerts significant influence on warpage deformation, exhibiting nonlinear variation trends. At low temperatures, warpage deformation is substantial; as mold temperature increases, warpage deformation rapidly diminishes. This indicates that reasonable elevation of mold temperature can prevent warpage deformation resulting from non-uniform cooling. Injection pressure demonstrates a pronounced influence on warpage deformation, displaying a descending trend. Higher injection pressure enables more uniform mold cavity filling, reducing internal stress differentials and thereby mitigating deformation risk. Injection speed exerts a modest influence on warpage deformation, presenting a gradual descending trend. Appropriately increasing injection speed facilitates deformation reduction by promoting uniform material filling and reducing non-uniform cooling risks. The packing pressure curve is relatively flat yet exhibits an initial decrease followed by an increase, indicating that appropriate packing pressure aids in warpage deformation reduction, while excessive packing pressure may induce additional internal stress accumulation.

Injection pressure exerts the most pronounced influence on mold core pin loading; excessive pressure may cause core pin bending or damage. The influence of injection

speed on core pin loading exhibits an initial ascending followed by a descending trend. Higher injection speeds may increase material impact forces, subjecting core pins to greater pressure; however, beyond a certain velocity threshold, pressure conversely decreases, potentially attributable to stabilization of material flow.

Integrating the analytical results from Pareto charts and main effects plots yields the following conclusions: Injection pressure and packing pressure exert the greatest influence on filling ratio and core pin loading, representing the most critical process parameters in HMN microfluidic chip injection molding. Elevated pressure facilitates material filling but increases core pin loading risk; consequently, optimization must balance these two factors. Warpage deformation correlates closely with mold temperature and injection pressure. Higher mold temperatures and moderate injection pressures facilitate warpage deformation reduction; however, excessively high temperatures or pressures must be avoided to prevent increased internal material stress and consequent deformation. Melt temperature significantly influences filling ratio, warpage deformation, and core pin loading. Elevated melt temperature enhances material flowability, reduces warpage deformation and filling defects, while simultaneously preventing excessive melt impact on core pins. Mold core pin loading is primarily influenced by injection pressure and injection speed. High injection pressure and speed substantially increase impact forces experienced by core pins; therefore, meticulous control of these two parameters is imperative to prevent mold core pin damage. To conduct multi-objective optimization, it is necessary to integrate the weights of filling ratio, warpage deformation (a surrogate indicator for residual stress), and core pin pressure, determining optimal parameter combinations based on the influence of process parameters on these responses. According to HMN application requirements, structural integrity represents a crucial guarantee of functionality. Although reducing core pin pressure can enhance mold longevity and safety, this ultimately depends on core pin material strength. Consequently, the assigned weights are: filling ratio (0.7), warpage deformation (0.2), and core pin pressure (0.1). Combining the importance of the aforementioned process parameters for response indicators, their influence trends, and weight allocations, the optimization direction and

response trends in this section are explicit and do not necessitate complex algorithms. Therefore, when prioritizing filling ratio while concurrently considering warpage deformation reduction and core pin pressure control, and based on the analytical results and selectable parameter ranges, the optimal injection molding parameter combination comprises: injection pressure 120–160 MPa, packing pressure 120–160 MPa, melt temperature 270–275°C, mold temperature 85–90°C, injection speed 40–50 cm^3/s, and packing time 1.5–2 s.

3.4 Molding quality of hollow microneedle array

Hollow microneedles must possess sufficient mechanical strength during skin penetration to prevent fracture or deformation. Compression testing is conducted on HMN arrays comprising 9 needles, with mechanical performance analyzed through time-force and displacement-force curves. The test results are presented in Figs. 3(g) and (h). The figures reveal that different samples exhibit similar force growth trends with increasing time during compression testing, which can be described as follows: The initial stage is characterized by a short duration and zero displacement, indicating that microneedles experience negligible deformation and substantial rigidity during early compression. The HMN array gradually begins deforming only when the average test pressure reaches 2.314 ± 0.163 N, indicating that each needle withstands an average force of 0.257 N without deformation—exceeding the 0.2 N force required for skin penetration and fully satisfying safe usage requirements. The second stage (Acceleration stage) is when the force increases rapidly with time, indicating that microneedles progressively experience loading and undergo deformation. This stage represents a critical mechanical response phase during microneedle compression, wherein samples experience substantial deformation while demonstrating favorable compressive stress tolerance. Application of approximately 21.52 N compression force produces merely 0.3 mm deformation, with each needle withstanding an average force of 2.39 N. Importantly, the deformation-force curve remains continuous and smooth, indicating continuous microneedle deformation throughout testing without brittle fracture, fully demonstrating HMN safety during use. Finally, the plateau stage is reached, where force gradually stabilizes as the microneedles approach their load-

bearing limit. At this point, the system enters a stable deformation state with force maintaining near peak values. Furthermore, mechanical performance across different samples exhibits close correspondence, indicating favorable consistency in the microneedle manufacturing process. The favorable linear relationship between force and increasing time and displacement reflects the rationality of HMN array structural design.

In Section 3.2, the results show that placing the HMN array at the far-gate position improved molding precision in the simulations (Fig. 2(d, e)), and this trend is further confirmed by the injection-molded HMN array shown in Fig. 4(a). In incompletely filled arrays, microneedles positioned closer to the cavity terminus achieve more complete filling and higher replication fidelity. The mechanisms underlying this phenomenon include: (1) During thin-walled micro-injection molding, viscous dissipation effects elevate melt flow front temperature, reducing melt viscosity and creating favorable conditions for HMN cavity filling. (2) When melt reaches the thin-walled cavity terminus, elevated melt temperature causes rapid pressure buildup within the cavity, thereby enhancing microstructure filling capability at the far-gate position. These phenomena concurrently validate conclusions from multi-objective optimization of injection processes, aligning to the fact that increasing injection pressure and packing pressure enhances HMN filling ratios. Statistical results for HMN height reveal an average height of ~688.2 ± 35.99 μm for the 9 hollow microneedles within the array, with an intra-part CV of 5.23%. In engineering practice, CV < 5% indicates excellent sample consistency, while HMN microfluidic chip injection molding achieves good consistency levels. Conversely, statistical analysis of 3 array groups yields an inter-batch CV of 0.76%, demonstrating exceptionally high sample consistency and reflecting the process stability advantages of HMN microfluidic chip injection molding. Characterization results for HMN base diameter, internal diameter, and inter-needle spacing are presented in Fig. 4(b). The average HMN base diameter is 503.5 ± 4.8 μm (design base diameter: 500 μm), and the average internal diameter is 237 ± 0 μm (design internal diameter: 240 μm), demonstrating high injection mold and molding precision. However, inter-needle spacing exhibits substantial fluctuation, with an average spacing

of only 40 ± 9.68 μm μm (design spacing: 60 μm). Based on the characterization results, the optimal injection process parameter combination comprises: injection speed 60 cm^3/s, injection pressure 1550 bar, packing pressure 1600 bar, melt temperature 280°C, mold temperature 90°C, and packing time 3 s.

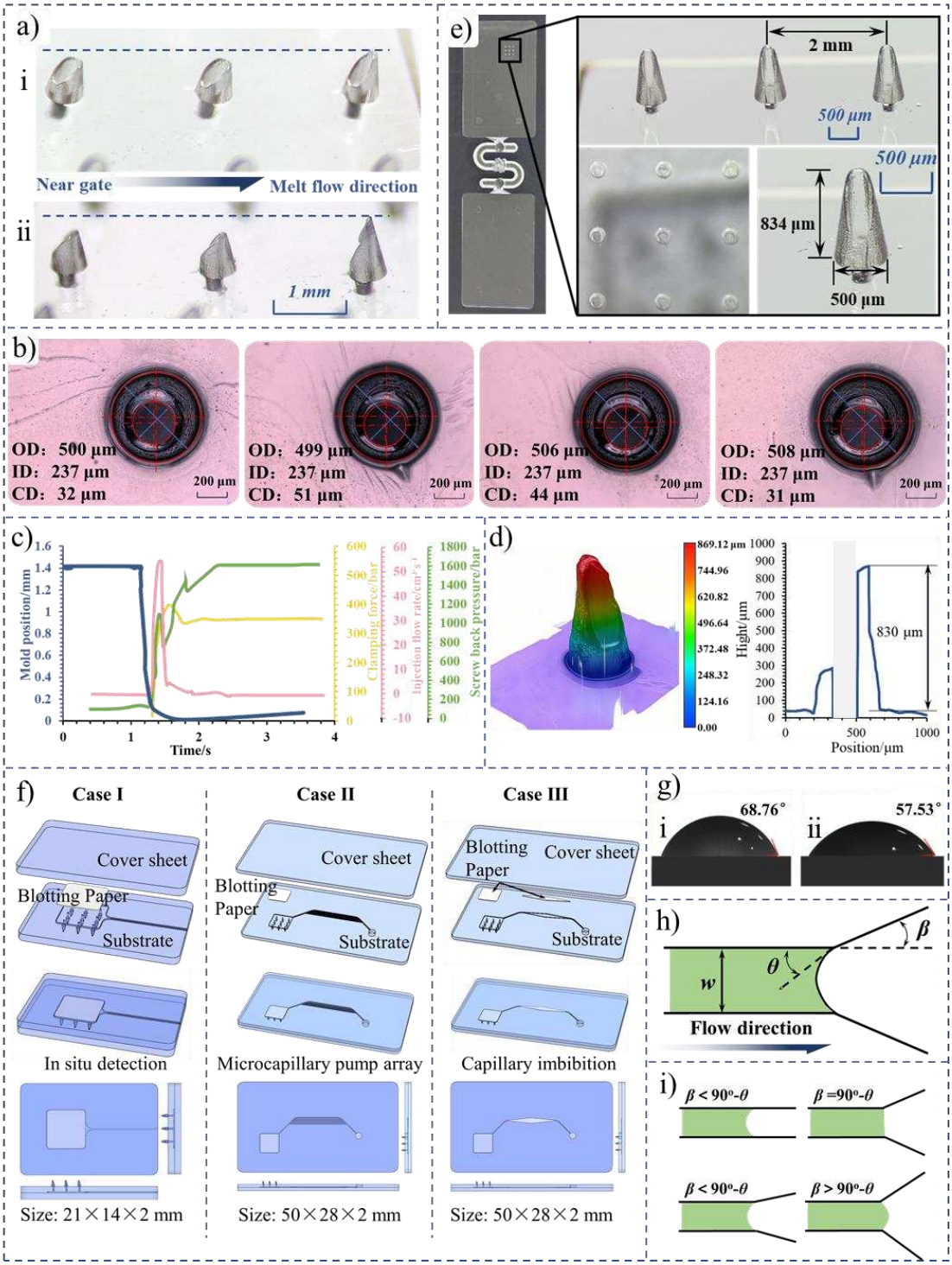


Fig. 4. Morphological characterization, dimensional analysis, and microfluidic integration of HMAs. (a) Effect of melt flow direction on microneedle morphology during injection molding. This

positional variation demonstrates the critical influence of runner design and gate location on replication fidelity across the array. (b) Microscopy images of hollow microneedles show dimensional measurements of key features. The outer and inner diameter of microneedles are accurate, and the size between mandrels fluctuates, which is mainly caused by machining positioning. (c) Multi-parameter process monitoring curves during a complete molding cycle. The graph displays temporal evolution of mold position (blue), clamping force (yellow), injection flow rate (pink), and screw back force (olive green). (d) Three-dimensional optical profilometry and height profile of a single microneedle, which visualizes the conical geometry with smooth surface topology. (e) Comprehensive morphological characterization of the μICM microneedle array. The high-fidelity replication across all features confirms the efficacy of the optimized μICM process. (f) Three microfluidic device configurations for different application scenarios. Case I: Compact design for in-situ detection. Case II: Passive fluid delivery via capillary action. Case III: The incorporated blotting paper to regulate flow rate. (g) Contact angle measurements of the fabricated HMN substrate using different testing media: (i) deionized water and (ii) artificial blood. (h) Schematic illustration of fluid flow behavior in a rectangular microchannel. (i) Four flow scenarios based on contact angle relationships at opposing channel walls.

Based on the optimal injection molding process parameter combination, the compression stage is introduced according to the process specifications in Table 1. The real-time injection machine parameter curves and the HMN ultra-depth characterization results are presented in Figs. 4(c) and (d). There, the actual injection machine compression distance exceeds the set value of 1 mm by ~0.4 mm. It is known that compression distance control precision primarily depends on the control precision of the injection machine's main hydraulic cylinder for mold closing position. Given the tonnage of the Arburg 370S precision injection machine, this positional accuracy is considered as ideal. Upon inspection, HMNs fabricated via injection-compression molding exhibit an average height of ~738.05 ± 67.11 μm with an intra-part CV of 8.57%, demonstrating favorable stability of the HMN microfluidic chip injection-compression molding. Compared to injection molding processes, the HMN height increases by approximately 6.75%, while injection pressure decreases from 1450 bar to 1300 bar (~10%), proving that injection-compression molding protects core pins while it enhances replication fidelity. Certain HMNs achieve heights up to 830 μm, with both average and maximum heights representing ideal dimensions for dermal ISF extraction, as illustrated in Fig. 4(e). The filling yield of the optimized HMN fabrication process is further evaluated over more than 50 micro-injection-compression molding cycles. Here, the filling yield is defined as the percentage of molded HMN arrays in which all

microneedles are formed to a stable size almost completely, with no significant defects such as incomplete filling, missing needles, or short-shot under optical inspection. According to this criterion, the optimized process achieves a filling yield above 94%, indicating good reproducibility for HMN array fabrication. Other well-formed HMN arrays and typical defects observed during process optimization, including incomplete filling and short-shot defects, are shown in Fig. S1.

3.5 ISF collection chip design and microelectrode bonding

Capillary action force is sufficient to meet ISF extraction requirements. However, its collection efficiency cannot match that of the external driving devices. Nevertheless, we need to ensure portability and ease of use of the entire driving apparatus, thus the capillary-driven systems possess unparalleled advantages for driving system design compactness and integration. To screen microfluidic structures suitable for different ISF sampling requirements, three chip configurations are designed and compared (see Fig. 4(f)): Case I, based on in-situ detection; Case II, based on comb-structured capillary pumps; and Case III, based on capillary diffusion principles. These designs are evaluated as candidate structures for rapid priming, passive delivery, and larger-volume collection.

Case I is designed based on in-situ detection, aiming to directly perform on-chip in-situ analysis of ISF extracted by microneedles, thereby reducing contamination and errors arising from sample transfer. Microneedles connect to a storage chamber that guides liquid to the detection region through capillary action. The detection region is positioned directly above the HMN array to minimize sample loss during flow. Due to its small volume and light weight, this design is suitable for rapid diagnostics and wearable applications requiring real-time analysis.

Case II employs a comb-structured capillary pump configuration, utilizing surface tension and capillary forces to propel ISF along specific pathways. The HMN array connects to the storage chamber through microchannels. Comb-structured capillary pumps are integrated along the microchannels to sustain liquid flow. The comb-shaped design of the capillary pump provides increased fluid contact area, facilitating sustained liquid flow and ensuring smooth liquid transport to the storage chamber.

Case III drives ISF flow within the chip through capillary diffusion. The liquid travels along microchannels from the HMN array to reach the storage chamber, which simultaneously functions as the detection chamber. The chip's HMN array connects to the storage chamber via microchannels designed to promote liquid diffusion and gradual transport. The device can exploit externally applied negative pressure or internal capillary action to enhance liquid flow, making it more suitable for prolonged continuous monitoring.

Whether HMN microfluidic chips can accomplish ISF extraction through capillary driving force depends critically on the hydrophilicity/hydrophobicity of chip materials. Prior to artificial blood extraction capability testing, contact angles between water and artificial blood with PMMA chips are measured (see Fig. 4(g)). The contact angles between water and artificial blood with PMMA chips are 68.76 ± 1.1° and 57.53 ± 1.3°, based on five repeated measurements. This shows that PMMA is a hydrophilic material possessing the fundamental capability to directly accomplish ISF extraction through capillary action. Compared to water, the chip exhibits greater capillary driving force for artificial blood, establishing a foundation for ISF extraction. In three-dimensional space, the liquid contact angle θ represents the angle between the liquid-solid interface and the liquid-gas interface in three-dimensional space. The expansion angle β affects the interfacial shape in the liquid advancing direction, which can be understood as the liquid's "effective contact angle" in three-dimensional space increasing by β, as illustrated in Fig. 4(h). In three-dimensional space, for liquid to continue advancing, its effective contact angle $\theta+\beta$ must be less than 90 degrees. That is:

$$\theta + \beta < 90^{o} \tag{4}$$

After adjusting, it will be：

$$\beta < 90^{o} - \theta \tag{5}$$

Consequently, when the expansion angle satisfies this condition $\beta < 90^{o} - \theta$, liquid can overcome capillary resistance to continue advancing. Otherwise, it will halt at the expansion point. In practical applications, when liquid flows from narrow channels to wide channels, capillary pressure decreases significantly due to increased channel

radius. If capillary pressure at this juncture is insufficient to overcome liquid viscous resistance and flow resistance, liquid will cease flowing at the interface, forming a stop valve, as illustrated in Fig. 4(i). At one end within the HMN lumen chip (β = 90°), absolute capillary stop valve conditions are constituted. Consequently, absorbent paper is placed within the HMN array region to modify this condition.

Bonding of these chips is entirely accomplished using patterned microelectrode bonding technology. This represents the first application of this novel microfluidic chip bonding technique to chips featuring complex microstructures rather than merely single-channel technical validation.

Among the three proposed application cases, chips differ in structural dimensions and microstructure distribution. Therefore, different microelectrode and bonding process combinations is designed according to chip structure. Microelectrode fabrication is carried out using the same mask-template-assisted electrodeposition route reported in our work [46], but with a geometry tailored to the present chip design. Briefly, a laser-patterned PET mask is used to define the microelectrode layout on a stainless-steel cathode, after which nickel is electrodeposited. The fabricated microelectrodes are further characterized by optical microscopy, 3D surface profilometry, infrared thermography, and four-point-probe conductivity measurements, confirming their dimensional fidelity, uniform morphology, stable heating behavior, and reproducible electrical performance. The detailed fabrication and characterization results are provided in Supplementary Fig. S2. According to different presentation schemes for ISF analysis platforms, the designed microelectrodes are illustrated in Fig. 5(a).

This experiment comparatively analyzed microelectrode design schemes for two different ISF extraction platforms, fabricating microelectrodes through electrodeposition processes followed by chip bonding. The objective is to evaluate the influence of different bonding processes on microelectrode structural integrity and bonding quality. Microelectrodes fabricated via electrodeposition according to different bonding schemes are illustrated in Fig. 5(b). The figure demonstrates that depending to different microfluidic chip structures, varying quantities of microelectrodes can be deposited on identically sized (4-inch) stainless steel cathode plates. For chips based on

in-situ detection principles, at least 12 microelectrodes can be simultaneously formed. For chips based on capillary pump or diffusion principles, 7 microelectrodes can be formed per batch. Specifically, microelectrode fabrication efficiency varies with chip dimensions, sealing methods, and cathode plate size. Fig. 5(b) reveals that different microelectrodes exhibit sharp edges, smooth surfaces, and shapes fundamentally consistent with mask template designs, indicating well-controlled electrodeposition processing.

Chips bonded according to different dimensions and microelectrode bonding schemes are illustrated in Fig. 5(c). These images reflect differences in the physical appearance of bonded chips as well as the transparency and boundary clarity of electrode regions. Experimental results further indicate that increasing chip dimensions negatively affects bonding uniformity and strength. Due to their larger area, larger chips are prone to temperature gradients during molten material cooling, causing non-uniform stress distribution and thereby affecting bonding uniformity. Small-dimension chips perform favorably in this regard, exhibiting virtually no visible bubbles or voids after bonding. Simple-structure electrode designs are more suitable for fusion bonding processes, since their short and regular flow channels enable better control and avoidance of thermal stress concentration phenomena during bonding. Complex-structure electrode designs require more precise electrode fabrication processes and dimensional control.

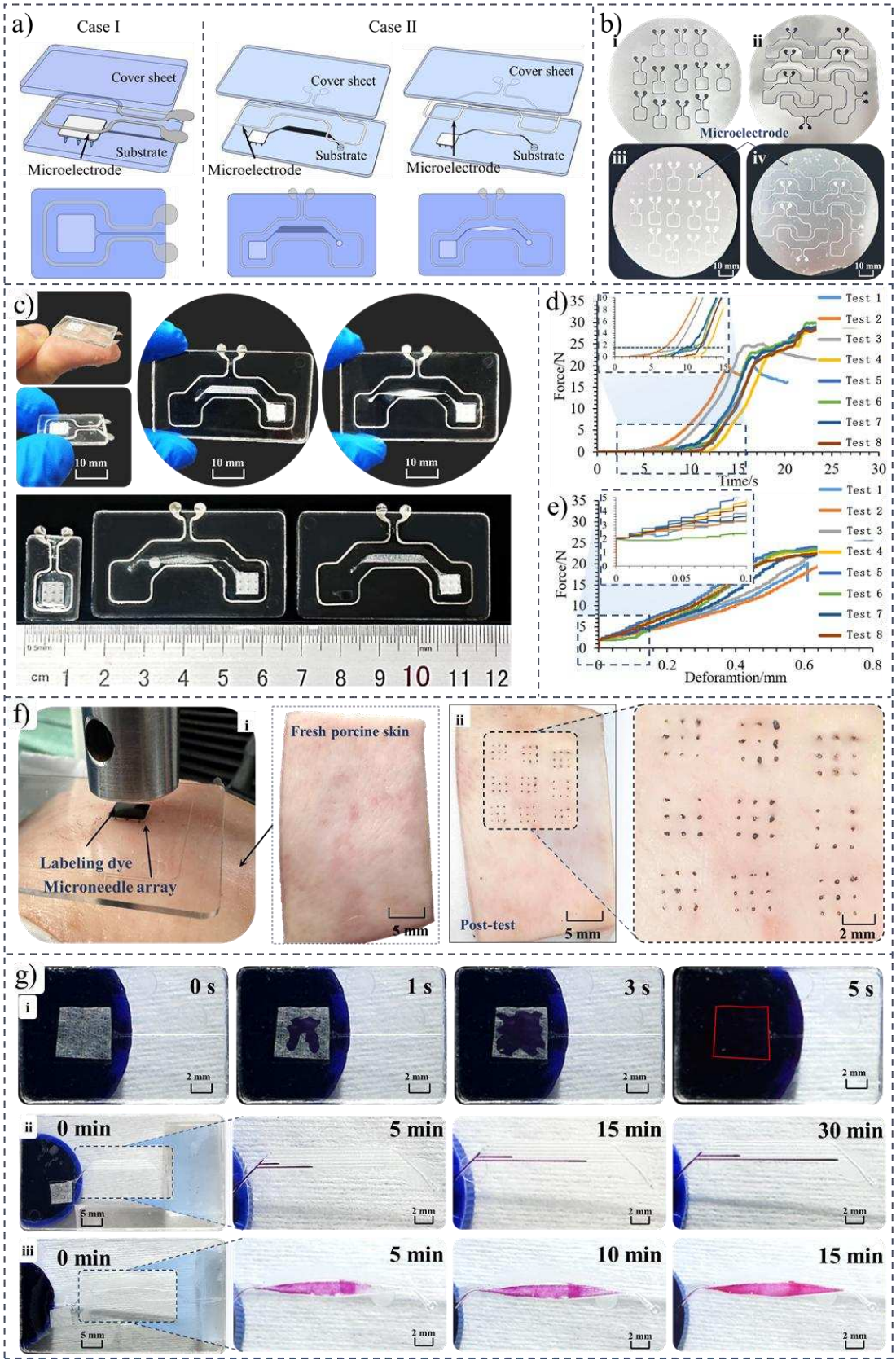


Fig. 5. Integrated microfluidic-microelectrode platform and in ex vivo validation of microneedle array performance. (a) Microelectrode bonding schemes with different chip structures. (b) Different types of masks and microelectrodes showcase strategies for the electrodeposition fabrication of

patterned microelectrodes. (c) Comparison of appearance and dimensions of HMN-based ISF extraction platform after microelectrode bonding. (d) Mechanical porcine skin insertion force-time curves for eight replicate tests. The narrow distribution of peak forces demonstrates excellent mechanical reproducibility essential for reliable clinical application. (e) Force-displacement relationships during porcine skin insertion. The consistent mechanical response confirms uniform array geometry and predictable penetration dynamics across multiple samples. (f) Ex vivo penetration testing on fresh porcine skin. The clean, uniform penetration marks without surrounding tissue damage confirm successful microneedle insertion and withdrawal, validating the mechanical design for transdermal applications. (g) Time-resolved visualization of passive liquid transport in three chip configurations. (i) Rapid filling of the in-situ detection cavity. (ii) Passive capillary-driven transport in the comb-structured capillary pump over 30 min. (iii) Enhanced passive collection using blotting paper as an auxiliary capillary-driving component over 15 min. The results compare the priming behavior, transport stability, and relative collection capacity of the three candidate designs under an abundant artificial blood supply.

Furthermore, microelectrodes of different dimensions exhibit differences in bonding process parameters. Bonding experimental results reveal that Case I achieves an average bonding voltage of 2.3 V, while Case II requires 3 V, with bonding time and bonding pressure both at 40 s and 80 kPa, respectively. According to Joule's law, when current passes through a resistor, the generated heat Q is proportional to the product of current I, resistance R, and time t. For smaller electrodes with identical cross-sectional area and shorter length, resistance is relatively lower. Evidently, the small electrodes of Case I can reach equivalent bonding temperatures at lower voltages. Lower process parameter levels imply potentially easier implementation with superior process windows and repeatability.

To further assess the manufacturability of the proposed platform, fabrication time and preliminary economic cost are considered. The validation mold used in this work is a two-cavity mold that produced the molded components required for one complete device per injection cycle. The mold fabrication cost is approximately US$3,550, and the injection molding cycle time is 35 s. For industrial production, especially for the compact Case I structure, the mold could be redesigned with tens of cavities to enable parallel production. This would reduce the effective molding time per device to the order of seconds to tens of seconds. In addition, the mold cost would be amortized over the total production volume, causing the mold-related cost per device to decrease substantially with scale.

The laboratory-scale microelectrode fabrication process currently requires approximately 5 min per electrode. However, this process is compatible with batch electrodeposition, and the unit fabrication time and cost could be further reduced through parallel processing and automated handling. Excluding equipment depreciation, labor, packaging, sterilization, quality-control rejection, regulatory validation, and supply-chain costs, the scaled consumable and process cost of the Case I device is expected to be on the order of several tens of cents per unit.

3.6 Interstitial Fluid Collection Application Performance Analysis

Transdermal staining methodology is employed to evaluate the skin penetration performance of HMN arrays. Single-array mechanical testing results from 8 replicates are presented in Fig. 5(d-e). Based on these results, the penetration process can be divided into two functional stages. In the initial stage, force values across all test curves remain relatively low (within 2 N). At this juncture, microneedles can be initiating contact with porcine skin. This stage is characterized by short duration and negligible displacement, indicating that notable porcine skin penetration has not yet occurred. The second stage (acceleration stage) begins when the average test force reaches 2.05 ± 0.02 N and the compression tester gradually detects displacement, indicating that the microneedles have penetrated the porcine skin. At this point, each needle withstands an average force of 0.228 N (comparable to the reported porcine skin penetration force of 0.21 N). The average force at which HMN deformation occurs is 0.257 ± 0.024 N, clearly demonstrating that HMNs can penetrate skin without undergoing deformation. During this stage, most experimental curves exhibit steep ascending trends, corresponding to deeper microneedle penetration with increasing force due to resistance encountered from deeper skin tissue layers. With increasing penetration depth, force values rise significantly, reflecting progressive HMN array insertion into skin and the resulting greater deformation resistance. At this stage, curve distributions among different experimental groups become more dispersed, revealing differences in force responses under varying penetration conditions. For example, Test 2 exhibits a sudden force increase during the intermediate stage, while Test 6 shows a more gradual force elevation. Notably, after multiple repeated porcine skin insertion tests, the HMN array

exhibits no significant deformation or fracture, clearly demonstrating sufficient mechanical strength and performance for skin penetration.

Fig. 5(f) presents the morphology before and after penetration staining experiments on porcine skin using HMN arrays. Ink penetrates skin tissue, by observing post-penetration staining patterns, one can determine whether successful penetration occurred in each attempt. To quantitatively assess penetration performance, mathematical statistical methods are utilized to analyze staining success rates across 9 replicate penetration experiments, evaluating HMN effectiveness and penetration consistency. Statistical results reveal that among 81 total test points, 77 exhibited successful staining (4 failed). yielding a success rate of ~95%. This demonstrates that the HMN array exhibits high repeatability and consistency in penetration behavior within porcine skin. Despite the high overall success rate, 4 penetration points failed to achieve successful staining, primarily occurring in Tests 4, 6, and 7. Potential causes of localized penetration failure include local non-uniformities in porcine skin surface characteristics such as thickness, and hardness, which may increase penetration difficulty in certain regions and prevent successful tissue puncture.

Next, we performed experiments using microfluidic chips with three different structural designs to test artificial blood extraction performance. It should be noted that this experiment is designed to compare passive transport and collection behavior under an abundant artificial blood supply. Therefore, the time scale in Fig. 5(g) should not be interpreted as the time scale for in vivo dynamic monitoring, which would require time-resolved ISF collection validation. During the experiments, all chips had identical materials, microneedle geometries, and microfluidic channel designs to ensure result comparability. Notably, the testing experiment provides abundant artificial blood supply. In in vivo applications, however, ISF typically requires extended time to accumulate toward the HMN region. Consequently, time results from extraction capability comparison experiments cannot be used to evaluate in vivo application timescales. Nevertheless, comparing absorption efficiency and optimizing microfluidic chip structures to enhance absorption stability remains beneficial. Sampling is conducted at 0, 1, 3, 5, 300, 600, 900, and 1800 s post-experiment initiation to observe and record

ISF extraction status at different time points. The test results are presented in Fig. 5(g). For the in-situ detection scheme, artificial blood is observed to have flowed into and completely filled the entire HMN posterior cavity within 5 s, demonstrating rapid liquid absorption velocity, which clearly demonstrates its suitability for POCT and micro-volume analysis applications.

The comb-structured capillary pump also fills the entire HMN posterior cavity by 5 s. However, during the subsequent 5-minute interval, noticeable liquid inflow phenomena gradually emerge at the comb-structured capillary pump location. By 15 min, liquid coverage length along the channel increases. Even after 30 min, the third and upper capillary branches remains largely unfilled. This behavior can be attributed to preferential flow through the lower pathways, which provides lower hydraulic resistance and a more continuous capillary pressure gradient. After the lower branches were filled, the remaining capillary pressure was insufficient to overcome the entry resistance, contact-line pinning, and possible air retention at the upper branch entrances. These results indicate that the vertically arranged parallel capillary structure is not essential for the final chip design and may introduce non-uniform flow distribution.

For the capillary diffusion scheme, liquid inflow into the diffusion region is clearly observed within 5 min, approaching maximum extraction volume within 10 min and stabilizing after 15 min. The dual-driving mechanism (capillary force and diffusion force) of the capillary diffusion pump scheme effectively enhances liquid collection efficiency while enabling collection of relatively large liquid volumes without external pumps. It possesses evident advantages in rapid sampling applications.

To further evaluate the applicability of the HMN platform under in vivo skin conditions, ISF extraction is performed on mouse dorsal skin using the Case I. The HMN collection patch is attached to the shaved dorsal skin (Fig. S3 (a, b)). At the beginning of the test, no visible liquid accumulation was observed in the collection region. After 10 min, liquid gradually appeared in the collection chamber, and further accumulation was observed after 30 min. These results demonstrate that the Case I can extract ISF from living skin under short-term in vivo conditions. The local skin response after device removal is also examined. Immediately after patch removal, localized insertion marks

were visible within the treated area (Fig. S3 (c)). These marks gradually weakened within 1-30 min, and no obvious macroscopic bleeding was observed during the recovery period. This rapid visual recovery indicates that the HMN insertion caused only limited short-term skin disruption under the tested conditions. Together with the ex vivo porcine skin insertion results and artificial blood transport experiments, the in vivo mouse study provides additional evidence supporting the feasibility of the HMN platform for ISF collection. H&E-stained cross-sections further confirmed localized penetration tracks at the insertion sites (Fig. S3 (d)), supporting the ability of the HMNs to penetrate skin tissue and establish an extraction pathway for ISF collection. Although the in vivo mouse experiment strengthens the evidence for short-term ISF extraction, it should not be interpreted as full validation of long-term wearable use. Practical long-term application will require further evaluation of repeated insertion, adhesion stability, motion-induced disturbance, skin irritation, infection risk and sampling stability over extended periods. In addition, the present work focuses on the manufacturing and functional validation of the ISF extraction prototype. Quantitative sensing will require integration with an analyte-specific electrochemical or optical transduction module, followed by calibration, selectivity, interference, drift and long-term stability tests. These issues will be addressed in future work toward a fully integrated ISF sensing platform.

In summary, the three chip designs show distinct passive transport behaviors. Case I is suitable for rapid priming and micro-volume in-situ detection. Case II increases the available capillary transport area but shows non-uniform filling in the vertically arranged parallel channels. Case III provides faster and more stable passive collection under the tested conditions, making it the preferred configuration for subsequent larger-volume ISF collection applications.

4 Conclusions and prospects

In this work, we systematically investigated the influence of mold structural design, gating system layout, and process parameters on HMN array molding quality. We discovered that positioning HMN arrays at far-gate locations substantially improves filling performance. The mechanism underlying this counterintuitive phenomenon is as

follows: melt at distal regions experiences longer flow paths, where viscous dissipation elevates polymer temperature, leading to lower viscosity. Simultaneously, more rapid melt pressure elevation is achieved, which promotes complete microstructure filling. More importantly, this layout effectively reduces impact forces experienced by core pins, thereby extending the mold's service life. When optimizing microstructure injection molding processes, the interconnected effects of multiple parameters on different performance indicators must be comprehensively considered. This approach resolves critical issues such as incomplete filling and poor molding stability of HMN arrays during injection molding. The discovery of enhanced distal microstructure molding capability expands micro-injection molding theory and provides novel design insights for molding high-aspect-ratio microstructures. The scalability analysis further indicates that multi-cavity mold design and batch microelectrode fabrication could support low-cost and high-throughput production of HMN-based ISF collection devices. Additionally, we proposed a design scheme for ISF extraction HMN microfluidic chips and developed a fabrication process for ISF microfluidic platforms. HMNs with heights of ~800 μm enable safe ISF collection with success rates of ~95%. Our chips were fabricated using patterned microelectrode bonding processes, which simultaneously validated the microelectrode fabrication process and its application in complex microchannel sealing. This technology is applicable to ISF collection platforms designed based on in-situ detection principles. Compared to negative pressure devices or capillary pump designs, in-situ detection demonstrates significant advantages in time efficiency and effectiveness.

In summary, this work demonstrates the feasibility of scalable fabrication and application of HMN-based health monitoring chips. Future integration of bonding electrodes with detection electrodes or enhancement of their versatility would substantially expand the scope of microfluidic chip applications in biomedical domains.

ACKNOWLEDGEMENTS

The authors acknowledge the financial support given by the National Natural Science Foundation of China (Normal project (No. 52575469 and 51875582), Young Scientists Fund (52605646) and Key International (Regional) Joint Research Program (No.

51920105008)), the Natural Science Foundation of Hunan province (Key research and development plan, No. 2026QK3016), and the Huxiang Young Talents Program of Hunan Province (No. 2019RS2003).

CONFLICT OF INTEREST

The authors declare no conflict of interest.

ETHICAL STATEMENT

All animal experiments were approved by the Institutional Animal Care and Use Committee of Dr.Can Biotechnology(Zhejiang) Co., Ltd. (Approval No. DRK-20260702042, dated [2026-07-02]). The study adhered to the guidelines set by the committee.

DATA AVAILABILITY

All data included in this study are available upon request by contact with the corresponding author.

REFERENCES

[1] J. Li, M. Wei, B. Gao, A Review of Recent Advances in Microneedle-Based Sensing within the Dermal ISF That Could Transform Medical Testing, ACS Sens. 9 (2024) 1149–1161. https://doi.org/10.1021/acssensors.4c00142.

[2] H.W. Wang, C. Liu, T.T. Feng, Y.F. Zhang, Y.F. Wu, Z. Dai, C.Q. Yi, Enzyme-Based Electrochemical Sensing Systems for On-Site Detection: Recent Progress and Prospects, SMALL 21 (2025). https://doi.org/10.1002/smll.202507926.

[3] S.J. Li, Y. Zhang, J.X. Liu, X. Wang, C.E. Qian, J.J. Wang, L.Q. Wu, C.X. Dai, H.J. Yuan, C. Wan, J.S. Li, W. Du, X.J. Feng, Y.W. Li, P. Chen, B.F. Liu, Fully Integrated and High-Throughput Microfluidic System for Multiplexed Point-Of-Care Testing, SMALL 20 (2024). https://doi.org/10.1002/smll.202401848.

[4] A. Sajeevan, R.A. Sukumaran, L.R. Panicker, Y.G. Kotagiri, Trends in ready-to-use portable electrochemical sensing devices for healthcare diagnosis, MICROCHIMICA ACTA 192 (2025). https://doi.org/10.1007/s00604-024-06916-x.

[5] B. Yang, X. Jiang, X. Fang, J. Kong, Wearable chem-biosensing devices: from basic research to commercial market, Lab Chip 21 (2021) 4285–4310. https://doi.org/10.1039/D1LC00438G.

[6] H.Y. Sun, Y.B. Zheng, G.Y. Shi, H. Haick, M. Zhang, Wearable Clinic: From Microneedle-Based Sensors to Next-Generation Healthcare Platforms, SMALL 19 (2023). https://doi.org/10.1002/smll.202207539.

[7] Y.S. Pang, Y.Y. Li, K.R. Chen, M. Wu, J.X. Zhang, Y.P. Sun, Y.R. Xu, X.L. Wang, Q. Wang, X.H. Ning, D.S. Kong, Porous Microneedles Through Direct Ink Drawing with Nanocomposite Inks for Transdermal Collection of Interstitial Fluid, SMALL 20 (2024). https://doi.org/10.1002/smll.202305838.

[8] R.M. Taylor, D. Maharjan, F. Moreu, J.T. Baca, Parametric study of 3D printed microneedle (MN) holders for interstitial fluid (ISF) extraction, MICROSYSTEM TECHNOLOGIES-MICRO-AND NANOSYSTEMS-INFORMATION STORAGE AND PROCESSING SYSTEMS 26 (2020) 2067–2073. https://doi.org/10.1007/s00542-020-04758-0.

[9] S. Ma, J. Li, L. Pei, N. Feng, Y. Zhang, Microneedle-based interstitial fluid extraction for drug analysis: Advances, challenges, and prospects, J. Pharm. Anal. 13 (2023) 111–126. https://doi.org/10.1016/j.jpha.2022.12.004.

[10] J. Yang, R. Luo, X.H. Yang Yong, Microneedle-Integrated Sensors for Extraction of Skin Interstitial Fluid and Metabolic Analysis, Int. J. Mol. Sci. 24 (2023).

[11] R. Omar, Y. Zheng, J. Wang, H. Haick, Microneedle Sensors for Multiplex Applications: Toward Advanced Biomedical and Environmental Analysis, Advanced Sensor Research 2 (2023) 2200032. https://doi.org/https://doi.org/10.1002/adsr.202200032.

[12] P.R. Miller, R.M. Taylor, B.Q. Tran, G. Boyd, T. Glaros, V.H. Chavez, R. Krishnakumar, A. Sinha, K. Poorey, K.P. Williams, S.S. Branda, J.T. Baca, R. Polsky, Extraction and biomolecular analysis of dermal interstitial fluid collected with hollow microneedles, Commun. Biol. 1 (2018) 173. https://doi.org/10.1038/s42003-018-0170-z.

[13] E. Kemp, T. Palomäki, I.A. Ruuth, Z.A. Boeva, T.A. Nurminen, R.T. Vänskä, L.K. Zschaechner, A.G. Pérez, T.A. Hakala, M. Wardale, E. Haeggström, J. Bobacka, Influence of enzyme immobilization and skin-sensor interface on non-invasive glucose determination from interstitial fluid obtained by magnetohydrodynamic extraction, Biosens. Bioelectron. 206 (2022) 114123. https://doi.org/https://doi.org/10.1016/j.bios.2022.114123.

[14] M. Friedel, I.A.P. Thompson, G. Kasting, R. Polsky, D. Cunningham, H.T. Soh, J. Heikenfeld, Opportunities and challenges in the diagnostic utility of dermal interstitial fluid, Nat. Biomed. Eng. 7 (2023) 1541–1555. https://doi.org/10.1038/s41551-022-00998-9.

[15] Z. Wu, Z. Qiao, S. Chen, S. Fan, Y. Liu, J. Qi, C.T. Lim, Interstitial fluid-based wearable biosensors for minimally invasive healthcare and biomedical applications, Commun. Mater. 5 (2024) 33. https://doi.org/10.1038/s43246-024-00468-6.

[16] H. Huma, M. Shabbir, S.E. Seo, O.S. Kwon, Frontiers in Point-of-Care Testing, Applied Science and Convergence Technology 33 (2024) 117–125. https://doi.org/10.5757/ASCT.2024.33.5.117.

[17] P.P. Samant, M.M. Niedzwiecki, N. Raviele, V. Tran, J. Mena-Lapaix, D.I. Walker, E.I. Felner, D.P. Jones, G.W. Miller, M.R. Prausnitz, Sampling interstitial fluid from human skin using a microneedle patch, Sci. Transl. Med. 12 (2020) eaaw0285. https://doi.org/10.1126/scitranslmed.aaw0285.

[18] T. Abbasiasl, S. Sarıca, U.C. Yener, E. Yilgor, I. Yilgor, H. Ceylan Koydemir, E. Öztürk, L. Beker, A Hydrophilic Hollow Microneedle Platform for Sampling Interstitial Fluid and On-Site Biomarker Detection, Adv. Mater. Technol. 10 (2025) e00891. https://doi.org/https://doi.org/10.1002/admt.202500891.

[19] Y. Yu, S. Liu, Z. Meng, X. Dong, J. Lao, Y. Wang, Macroporous-channel hollow microneedles enable vacuum-free interstitial fluid sampling and on-patch sensing, Acta Biomater. 214 (2026) 572–583. https://doi.org/https://doi.org/10.1016/j.actbio.2026.03.028.

[20] Mark R. Prausnitz, Engineering Microneedle Patches for Vaccination and Drug Delivery to Skin, Annu. Rev. Chem. Biomol. Eng 8 (2017) 177–200. https://doi.org/10.1146/annurev-chembioeng-060816-101514.

[21] D.W. Bodhale, A. Nisar, N. Afzulpurkar, Structural and microfluidic analysis of hollow side-open polymeric microneedles for transdermal drug delivery applications, Microfluid. Nanofluidics 8 (2010) 373–392. https://doi.org/10.1007/s10404-009-0467-9.

[22] A. Ahmadpour, P.K. Isgor, B. Ural, B.N. Eren, M.R. Sarabi, M. Muradoglu, S. Tasoglu, Microneedle arrays integrated with microfluidic systems: Emerging applications and fluid flow modeling, Biomicrofluidics 17 (2023) 021501. https://doi.org/10.1063/5.0121578.

[23] K. Takeuchi, N. Takama, K. Sharma, O. Paul, P. Ruther, T. Suga, B. Kim, Microfluidic chip connected to porous microneedle array for continuous ISF sampling, Drug Deliv. Transl. Res. 12 (2022) 435–443. https://doi.org/10.1007/s13346-021-01050-0.

[24] K.M. Saifullah, Z. Faraji Rad, Sampling Dermal Interstitial Fluid Using Microneedles: A Review of Recent Developments in Sampling Methods and Microneedle-Based Biosensors, Adv. Mater. Interfaces 10 (2023) 2201763. https://doi.org/https://doi.org/10.1002/admi.202201763.

[25] H. Teymourian, A. Barfidokht, J. Wang, Electrochemical glucose sensors in diabetes management: an updated review (2010–2020), Chem. Soc. Rev. 49 (2020) 7671–7709. https://doi.org/10.1039/D0CS00304B.

[26] Z. Zhen, C. Pan, L. Kegang, E. Carlos, A Versatile Bonding Method for PDMS and SU-8 and Its Application towards a Multifunctional Microfluidic Device, Micromachines (Basel). 7 (2016) 230.

[27] L. Pan, W. Wu, J. Liu, X. Li, Ultrasonic Plasticization Microinjection Precision Molding of Polypropylene Microneedle Arrays, ACS Appl. Polym. Mater. 5 (2023) 9354–9363. https://doi.org/10.1021/acsapm.3c01844.

[28] Y. Li, H. Zhang, R. Yang, Y. Laffitte, U. Schmill, W. Hu, M. Kaddoura, E.J.M. Blondeel, B. Cui, Fabrication of sharp silicon hollow microneedles by deep-reactive ion etching towards minimally invasive diagnostics, Microsyst. Nanoeng. 5 (2019) 41. https://doi.org/10.1038/s41378-019-0077-y.

[29] H.R. Nejad, A. Sadeqi, G. Kiaee, S. Sonkusale, Low-cost and cleanroom-free fabrication of microneedles, Microsyst. Nanoeng. 4 (2018) 17073. https://doi.org/10.1038/micronano.2017.73.

[30] P.C. Wang, S.J. Paik, S. Chen, S. Rajaraman, Fabrication and Characterization of Polymer Hollow Microneedle Array Using UV Lithography Into Micromolds, Journal of Microelectromechanical Systems 22 (2013) 1041–1053.

[31] Z. Faraji Rad, P.D. Prewett, G.J. Davies, High-resolution two-photon polymerization: the most versatile technique for the fabrication of microneedle arrays, Microsyst. Nanoeng. 7 (2021) 71. https://doi.org/10.1038/s41378-021-00298-3.

[32] H. Zhang, H. Liu, N. Zhang, A Review of Microinjection Moulding of Polymeric Micro Devices, Micromachines (Basel). 13 (2022). https://doi.org/10.3390/mi13091530.

[33] M. Gülçür, E. Brown, T. Gough, B. Whiteside, Characterisation of microneedle replication and flow behaviour in ultrasonic micro-injection moulding through design of experiments, J. Manuf. Process. 102 (2023) 513–527. https://doi.org/10.1016/j.jmapro.2023.07.068.

[34] B. Zhao, F. Mo, W. Wu, B. Jiang, G. Ziegmann, Deformation patterns and coordination mechanisms of cross-size microchannels during thermocompression bonding process, Journal of Materials Research and Technology 26 (2023) 3701–3709. https://doi.org/10.1016/j.jmrt.2023.08.141.

[35] P. Azarikhah, A. Mushtaq, K.M. Saifullah, P.D. Prewett, G.J. Davies, Z. Faraji Rad, A critical review of advances and challenges in microinjection moulding of polymeric microneedles, J. Drug Deliv. Sci. Technol. 114 (2025) 107435. https://doi.org/https://doi.org/10.1016/j.jddst.2025.107435.

[36] D. Masato, M. Sorgato, G. Lucchetta, Analysis of the influence of part thickness on the replication of micro-structured surfaces by injection molding, Mater. Des. 95 (2016) 219–224. https://doi.org/https://doi.org/10.1016/j.matdes.2016.01.115.

[37] H.R. Nejad, A. Sadeqi, G. Kiaee, S. Sonkusale, Low-cost and cleanroom-free fabrication of microneedles, Microsyst. Nanoeng. 4 (2018) 17073. https://doi.org/10.1038/micronano.2017.73.

[38] M. Tromm, V. Shaayegan, C. Wang, H.-P. Heim, C.B. Park, Investigation of the mold-filling phenomenon in high-pressure foam injection molding and its effects on the cellular structure in expanded foams, Polymer. 160 (2019) 43–52. https://doi.org/https://doi.org/10.1016/j.polymer.2018.11.006.

[39] D. Masato, M. Sorgato, G. Lucchetta, Characterization of the micro injection-compression molding process for the replication of high aspect ratio micro-structured surfaces, Microsystem Technologies 23 (2017) 3661–3670. https://doi.org/10.1007/s00542-016-3149-z.

[40] W. Yu, J. Gu, Z. Li, S. Ruan, B. Chen, C. Shen, L.J. Lee, X. Wang, Study on the Influence of Microinjection Molding Processing Parameters on Replication Quality of Polylactic Acid Microneedle Array Product, Polymers (Basel). 15 (2023). https://doi.org/10.3390/polym15051199.

[41] F. Sammoura, J. Kang, Y.-M. Heo, T. Jung, L. Lin, Polymeric microneedle fabrication using a microinjection molding technique, Microsystem Technologies 13 (2007) 517–522. https://doi.org/10.1007/s00542-006-0204-1.

[42] B. Zhao, D. Kontziampasis, Z. Yang, B. Jiang, W. Wu, D. Zhang, Tuning surface microtopography for optimum thermocompression bonding performance: structure, process parameters, and mechanisms on microfluidic chips, Mater. Des. 262 (2026). https://doi.org/10.1016/j.matdes.2026.115448.

[43] Y. Gong, J.M. Park, J. Lim, An Interference-Assisted Thermal Bonding Method for the Fabrication of Thermoplastic Microfluidic Devices, Micromachines (Basel). 7 (2016). https://doi.org/10.3390/mi7110211.

[44] K. Giri, C.-W. Tsao, Recent Advances in Thermoplastic Microfluidic Bonding, Micromachines (Basel). 13 (2022). https://doi.org/10.3390/mi13030486.

[45] B. Zhao, W. Wu, M. Zhou, B. Jiang, G. Ziegmann, Highly dynamic tempered in-mold thermocompression bonding of microfluidic chips: process characteristics and bonding performances, Journal of Materials Research and Technology 24 (2023) 639–652. https://doi.org/10.1016/j.jmrt.2023.03.040.

[46] B. Zhao, D. Kontziampasis, L. Huang, W. Wu, B. Jiang, An innovative patternable microelectrode bonding technology for high-performance and cost-effective sealing in microfluidic chips, Chemical Engineering Journal 503 (2025) 158214. https://doi.org/https://doi.org/10.1016/j.cej.2024.158214.

[47] A. Olanrewaju, M. Beaugrand, M. Yafia, D. Juncker, Capillary microfluidics in microchannels: from microfluidic networks to capillaric circuits, Lab Chip 18 (2018) 2323–

2347. https://doi.org/10.1039/C8LC00458G.
[48] E. Khanjani, A. Fergola, J.A. López Martínez, S. Nazarnezhad, J. Casals Terre, S.L. Marasso, B. Aghajanloo, Capillary microfluidics for diagnostic applications: fundamentals, mechanisms, and capillarics, Frontiers in Lab on a Chip Technologies 4 (2025). https://doi.org/10.3389/frlct.2025.1502127.
[49] X. Jiang, P.B. Lillehoj, Microneedle-based skin patch for blood-free rapid diagnostic testing, Microsyst. Nanoeng. 6 (2020) 96. https://doi.org/10.1038/s41378-020-00206-1.
[50] L.K. Vora, K. Moffatt, I.A. Tekko, A.J. Paredes, F. Volpe-Zanutto, D. Mishra, K. Peng, R.R.S. Thakur, R.F. Donnelly, Microneedle array systems for long-acting drug delivery, EUROPEAN JOURNAL OF PHARMACEUTICS AND BIOPHARMACEUTICS 159 (2021) 44–76. https://doi.org/10.1016/j.ejpb.2020.12.006.
[51] G.E. Flaten, Z. Palac, A. Engesland, J. Filipović-Grčić, Ž. Vanić, N. Škalko-Basnet, In vitro skin models as a tool in optimization of drug formulation, European Journal of Pharmaceutical Sciences 75 (2015) 10–24. https://doi.org/https://doi.org/10.1016/j.ejps.2015.02.018.
[52] J. Cheng, J. Huang, Q. Xiang, H. Dong, Hollow microneedle microfluidic paper-based chip for biomolecules rapid sampling and detection in interstitial fluid, Anal. Chim. Acta 1255 (2023) 341101. https://doi.org/https://doi.org/10.1016/j.aca.2023.341101.
[53] R. V Dixon, E. Skaria, W.M. Lau, P. Manning, M.A. Birch-Machin, S.M. Moghimi, K.W. Ng, Microneedle-based devices for point-of-care infectious disease diagnostics, Acta Pharm. Sin. B 11 (2021) 2344–2361. https://doi.org/https://doi.org/10.1016/j.apsb.2021.02.010.
[54] C.H. Ahn, J.-W. Choi, G. Beaucage, J.H. Nevin, J.-B. Lee, A. Puntambekar, J.Y. Lee, Disposable smart lab on a chip for point-of-care clinical diagnostics, Proceedings of the IEEE 92 (2004) 154–173. https://doi.org/10.1109/JPROC.2003.820548.
[55] J. Zhu, X. Zhou, H.-J. Kim, M. Qu, X. Jiang, K. Lee, L. Ren, Q. Wu, C. Wang, X. Zhu, P. Tebon, S. Zhang, J. Lee, N. Ashammakhi, S. Ahadian, M.R. Dokmeci, Z. Gu, W. Sun, A. Khademhosseini, Microneedle Patches: Gelatin Methacryloyl Microneedle Patches for Minimally Invasive Extraction of Skin Interstitial Fluid (Small 16/2020), Small 16 (2020) 2070086. https://doi.org/https://doi.org/10.1002/smll.202070086.
[56] L. Xu, A. Wang, X. Li, K.W. Oh, Passive micropumping in microfluidics for point-of-care testing, Biomicrofluidics 14 (2020) 031503. https://doi.org/10.1063/5.0002169.
[57] I. Atay, E. Yilgör, G. Neşer, T. Abbasiasl, M.B. Yagci, I. Yilgör, L. Beker, Critical Role of Surface Properties in Passive Interstitial Fluid Extraction Using Polymeric Hollow Microneedles for Wearable Diagnostics, Adv. Mater. Interfaces 12 (2025) 2500001. https://doi.org/https://doi.org/10.1002/admi.202500001.
[58] T. Elias Abi-Ramia Silva, S. Kohler, N. Bartzsch, F. Beuschlein, A.T. Güntner, 3D-printed polymer hollow microneedles on microfluidic platforms for minimally invasive interstitial fluid extraction, Cell Biomaterials 1 (2025) 100008. https://doi.org/https://doi.org/10.1016/j.celbio.2024.100008.
[59] Z. Faraji Rad, R.E. Nordon, C.J. Anthony, L. Bilston, P.D. Prewett, J.-Y. Arns, C.H. Arns, L. Zhang, G.J. Davies, High-fidelity replication of thermoplastic microneedles with open microfluidic channels, Microsyst. Nanoeng. 3 (2017) 17034. https://doi.org/10.1038/micronano.2017.34.
[60] T. Evens, L. Van Hileghem, F. Dal Dosso, J. Lammertyn, O. Malek, S. Castagne, D. Seveno,

A. Van Bael, Producing Hollow Polymer Microneedles Using Laser Ablated Molds in an Injection Molding Process, J. Micro Nanomanuf. 9 (2021). https://doi.org/10.1115/1.4051456.

[61] P. Makvandi, M. Kirkby, A.R.J. Hutton, M. Shabani, C.K.Y. Yiu, Z. Baghbantaraghdari, R. Jamaledin, M. Carlotti, B. Mazzolai, V. Mattoli, R.F. Donnelly, Engineering Microneedle Patches for Improved Penetration: Analysis, Skin Models and Factors Affecting Needle Insertion, Nanomicro Lett. 13 (2021) 93. https://doi.org/10.1007/s40820-021-00611-9.

[62] M.R. Prausnitz, R. Langer, Transdermal drug delivery., Nat. Biotechnol. 26 (2008) 1261–1268. https://doi.org/10.1038/nbt.1504.

[63] V. Planz, C.-M. Lehr, M. Windbergs, In vitro models for evaluating safety and efficacy of novel technologies for skin drug delivery., J. Control. Release 242 (2016) 89–104. https://doi.org/10.1016/j.jconrel.2016.09.002.

[64] R.F. Donnelly, M.J. Garland, D.I.J. Morrow, K. Migalska, T.R.R. Singh, R. Majithiya, A.D. Woolfson, Optical coherence tomography is a valuable tool in the study of the effects of microneedle geometry on skin penetration characteristics and in-skin dissolution, Journal of Controlled Release 147 (2010) 333–341. https://doi.org/https://doi.org/10.1016/j.jconrel.2010.08.008.

[65] H.S. Gill, D.D. Denson, B.A. Burris, M.R. Prausnitz, Effect of Microneedle Design on Pain in Human Volunteers, Clin. J. Pain 24 (2008).

[66] X. Xiu, G. Gao, Y. Liu, F. Ma, Drug delivery with dissolving microneedles: skin puncture, its influencing factors and improvement strategies, J. Drug Deliv. Sci. Technol. 76 (2022) 103653. https://doi.org/https://doi.org/10.1016/j.jddst.2022.103653.

[67] G.-S. Liu, Y. Kong, Y. Wang, Y. Luo, X. Fan, X. Xie, B.-R. Yang, M.X. Wu, Microneedles for transdermal diagnostics: Recent advances and new horizons, Biomaterials 232 (2020) 119740. https://doi.org/https://doi.org/10.1016/j.biomaterials.2019.119740.

[68] P. Aggarwal, C.R. Johnston, Geometrical effects in mechanical characterizing of microneedle for biomedical applications, Sens. Actuators B Chem. 102 (2004) 226–234. https://doi.org/https://doi.org/10.1016/j.snb.2004.04.024.

[69] G. Anbazhagan, S.B. Suseela, R. Sankararajan, Effect of hollow microneedle geometry structure on mechanical stability and microfluidic flow for transdermal drug delivery applications, Microfluid. Nanofluidics 27 (2023) 25. https://doi.org/10.1007/s10404-023-02636-5.

[70] M.S. Lhernould, Optimizing hollow microneedles arrays aimed at transdermal drug delivery, Microsystem Technologies 19 (2013) 1–8. https://doi.org/10.1007/s00542-012-1663-1.

[71] H.J.G.E. Gardeniers, R. Luttge, E.J.W. Berenschot, M.J. de Boer, S.Y. Yeshurun, M. Hefetz, R. van't Oever, A. van den Berg, Silicon micromachined hollow microneedles for transdermal liquid transport, Journal of Microelectromechanical Systems 12 (2003) 855–862. https://doi.org/10.1109/JMEMS.2003.820293.

[72] K.L. Yung, Y. Xu, C. Kang, H. Liu, K.F. Tam, S.M. Ko, F.Y. Kwan, T.M.H. Lee, Sharp tipped plastic hollow microneedle array by microinjection moulding, Journal of Micromechanics and Microengineering 22 (2012) 15016. https://doi.org/10.1088/0960-1317/22/1/015016.

[73] O. Olatunji, D.B. Das, M.J. Garland, L. Belaid, R.F. Donnelly, Influence of array interspacing on the force required for successful microneedle skin penetration: theoretical

and practical approaches., J. Pharm. Sci. 102 (2013) 1209–1221. https://doi.org/10.1002/jps.23439.

[74] K.L. Yung, Y. Xu, C. Kang, H. Liu, K.F. Tam, S.M. Ko, F.Y. Kwan, T.M.H. Lee, Sharp tipped plastic hollow microneedle array by microinjection moulding, Journal of Micromechanics and Microengineering 22 (2012) 015016. https://doi.org/10.1088/0960-1317/22/1/015016.

[75] C. C. Lin, T. C. Wu, Y. S. Chen, B.Y. Yang, A Semi-Analytical Method for Designing a Runner System of a Multi-Cavity Mold for Injection Molding, Polymers (Basel). 14 (2022). https://doi.org/10.3390/polym14245442.